Petroleum Science 23 (2026) 2655–2685

Contents lists available at ScienceDirect

Petroleum Science

journal homepage: www.keaipublishing.com/en/journals/petroleum-science

Original Paper

Lateral vibration and vibration control methods for ultra-deep well drill strings based on Cosserat geometrically exact beam theory

Fan Yu [a,b], Yun-Hu Lu [b,*], Yan Jin [b], Wei Li [c], Bing-Qian Lv [d], Hong-Jian Ni [e], Gen-Lu Huang [e]

[a] School of Petroleum, China University of Petroleum (Beijing) at Karamay, Karamay, 834000, Xinjiang, China
[b] School of Petroleum Engineering, China University of Petroleum (Beijing), Beijing, 102299, China
[c] Geosteering & Logging Research Institute, Sinopec Matrix Corporation, Qingdao, 266071, Shandong, China
[d] China Petroleum Materials Procurement Center, Karamay, 834000, Xinjiang, China
[e] School of Petroleum Engineering, China University of Petroleum (East China), Qingdao, 266580, Shandong, China

ARTICLE INFO

Article history:
Received 16 October 2025
Received in revised form
12 January 2026
Accepted 13 January 2026
Available online 18 January 2026

Edited by Jia-Jia Fei

Keywords:
Drill string dynamics
Geometrically exact beam
Ultra-deep well
Lateral vibration
Vibration suppression

ABSTRACT

In ultra-deep well operations, severe lateral vibration of drill string is a major factor in tool failure and decreased drilling efficiency. To investigate the vibration mechanisms and identify effective mitigation approaches, a dynamic model for lateral vibration in ultra-deep well drill strings was established using Cosserat geometrically exact beam theory. The model systematically examined the effects of rotational speed, WOB, and stabilizer position and size on the vibration behavior. Key findings were validated against downhole measurement data from ultra-deep wells. Additionally, two control strategies leveraging modal competition and transverse wave disturbance were proposed. Results indicate that the bottom hole assembly (BHA) is particularly prone to intense lateral vibrations, with its vibrational modes governed by rotational speed and WOB. When the WOB is below the critical buckling load, increasing either the rotational speed or WOB promotes backward whirling of the BHA, thereby intensifying the vibration severity and bending stress. Conversely, when the WOB exceeds the critical buckling load, the system transitions into a buckling–whirling competition mode, resulting in a significant reduction in the vibration intensity and bending stress. This trend was reasonably verified through field data. Artificially inducing this low-risk modal competition by adjusting the WOB and rotational speed can effectively reduce the probability of drill string failure. The motion of stabilizers shifts from forward whirling to backward whirling as the diameter decreases, which considerably alters the vibration-propagation patterns. The vibration-damping effects of both full-gauge and under-gauge stabilizers initially increase and then decrease as their installation position moves upward. Under-gauge stabilizers exhibit less consistent behavior under non-severe vibration conditions; nevertheless, they can suppress severe whirling by interfering with adjacent drill string vibrations through low-frequency transverse waves. They also demonstrate lower sensitivity to the installation position and enhance drill string safety through stress dispersion. Considering comprehensive vibration suppression, drill string integrity, and engineering applicability, installing under-gauge stabilizers can be a viable BHA optimization measure with significant practical value. This study provides a theoretical basis for vibration control in ultra-deep well drill strings, and the proposed strategy offers valuable insights for improving drilling efficiency and ensuring operational safety.

1. Introduction

Global oil and gas exploration has been advancing into deeper formations, driving rapid growth in ultra-deep (6000–9000 m) and extra-deep (>9000 m) wells. China's Tarim Oilfield has established Asia's deepest onshore oil field, including the Shenditake-1 well at a record depth of 10910 m. During deep drilling, the bottom hole assembly (BHA) and upper drill string

* Corresponding author.
E-mail address: luyh@cup.edu.cn (Y.-H. Lu).
Peer review under the responsibility of China University of Petroleum (Beijing).

https://doi.org/10.1016/j.petsci.2026.01.014

form a highly slender rotating system, which is subjected to extreme loads, including substantial axial forces, high torque, and high-pressure/high-temperature conditions. Constrained within narrow boreholes, their vibration characteristics are highly complex (Wang et al., 2024a). Severe vibrations not only jeopardize drill string integrity but also interfere with surface monitoring because of downhole signal attenuation (Nüsse et al., 2023; Zhang et al., 2023b). As a result, conservative drilling parameters and assemblies (such as pendulum assemblies) are often used, whereas active trajectory-control tools are limited by temperature and pressure (Gao and Huang, 2024; Li et al., 2024). These challenges collectively reduce the rate of penetration (ROP) and increase operational costs (Yi et al., 2024). Thus, downhole vibration emerges as a critical obstacle in deep drilling, necessitating the development of effective vibration-mitigation and efficiency-enhancement technologies.

The downhole drill strings exhibit multiple vibration types, including axial, lateral, and torsional (Zhang et al., 2024b). These vibrations manifest as destructive dynamics, such as bit bounce, stick-slip, whirling, and high-frequency torsional oscillations (Holsaeter et al., 2023). They are driven by factors such as bit-rock interactions, drill string eccentricity, wellbore friction, and periodic loads from impact tools (Cayeux and Ambrus, 2023; Di et al., 2024a). Significant progress in drill string dynamics modeling now enables effective simulation of these vibrations (Kamel et al., 2025). Among them, lateral vibrations have become a primary research focus owing to their severe consequences, multiple excitation mechanisms, and complex behavior (Ledgerwood et al., 2010). The established models for lateral vibration are generally categorized into lumped-parameter and continuous-parameter types (Faghihi et al., 2024; Huang et al., 2025).

Lumped-parameter models represent the drill string as a multi-degree-of-freedom system comprising concentrated masses, massless elastic segments (springs), and dampers (Christoforou and Yigit, 2003; Liu et al., 2013). They are widely used to investigate vibration mechanisms because of their moderate modeling complexity and high computational efficiency (Nüsse et al., 2024). The key findings from lateral vibration studies using lumped-parameter models include the following: 1) Gravity-induced radial component variations cause distinct whirling behaviors in vertical and deviated wells. Vertical wells typically exhibit non-contact revolution, forward whirling, irregular motion, and backward whirling, whereas deviated wells exhibit roll-slide oscillation, backward whirling, and transition states (Li et al., 2020; Wang et al., 2024b). 2) An increase in key parameters such as rotational speed, friction coefficient, mass eccentricity, and borehole clearance promotes a transition toward backward whirling (Kapitaniak et al., 2017; Stroud et al., 2011; Xie et al., 2020). Studies on coupled lateral vibrations by Moraes and Savi (2019) have demonstrated that axial vibrations (bit bounce) could induce whirling through the release of torsional energy. They found that vibrations could be suppressed by maintaining a constant WOB while first reducing and then increasing the rotational speed. In contrast, simultaneously increasing both the WOB and rotational speed did not mitigate whirling. Research by Leine et al. (2002) and Choe et al. (2023) indicated that stick-slip vibrations could excite drill string whirling; however, backward whirling and stick-slip vibrations were mutually exclusive. Huang et al. (2024, 2025) developed an integrated system that incorporated both drill string dynamics and bit-rock interactions via particle flow discrete-element modeling. This approach offers advantages over existing coupled dynamics models by providing a more realistic characterization of formation heterogeneity and bit geometry (Feng et al., 2017; Richard et al., 2007; Zhang et al., 2024a). It elucidates the fundamental mechanism by which backward whirling reduces the ROP: increased drill string-wellbore friction decreases the effective WOB at the bit-rock interface (Ni et al., 2025).

While lumped-parameter models have advanced the theoretical understanding of drill string dynamics and demonstrated accuracy in scaled experiments, they are fundamentally constrained compared with continuous-parameter approaches (Goicoechea et al., 2023, 2024b). First, by neglecting distributed inertial effects, these models cannot capture stress wave propagation, specifically, the phase delay in wave reflections. This limitation restricts their application to short structures where the rate of boundary condition change is slow relative to the propagation speed of internal stress waves. Second, as severe simplifications of continuum systems, lumped-parameter models fail to characterize complex dynamic behaviors, such as higher-order vibration modes, in actual drill strings.

Continuous-parameter models provide a more physically realistic representation of the drill string than their lumped-parameter counterparts by continuously distributing properties such as density and elastic modulus along the length. These models are subsequently discretized into elements, including shell, beam, or solid elements, which are then solved using numerical methods such as the finite-element method or finite-difference method. Building upon Heisig's (Heisig, 1993) Euler-Bernoulli beam formulation, progressive refinements have evolved it into a generalized beam-element framework (Al Dushaishi, 2015; Dykstra, 1996; Wilson, 2017; Zhang et al., 2024c). Theoretical and experimental studies have confirmed its computational versatility and engineering accuracy in drill string vibration analysis (Di et al., 2021; Wang et al., 2018; Xiang et al., 2023; Zhang et al., 2020). This approach preserves the dynamic pattern prediction capability of lumped-parameter models while effectively capturing complex vibrations through geometric nonlinearity. Furthermore, it has been applied to practical challenges involving the stress wave reflection effect, such as impact drag reduction (Liu et al., 2023).

However, in lateral vibration studies for ultra-deep wells, conventional beam-element models often produce over-simplified results. They typically predict severe vibrations localized at the BHA but offer limited insight into vibration control. This limitation stems from their mathematical framework, in which nodal-coordinate-based beam elements form geometrically inexact beams (Fang, 2016). Such models require the deformed configurations to remain near the reference configuration. Even with nonlinear strain-displacement relationships, they impose strict constraints on centroid displacements and cross-section rotations relative to the reference frame (Di et al., 2024b; Zhu et al., 2024). Consequently, they exhibit significant errors under the large bending and torsional deformations characteristic of complex deep well conditions (Shabana et al., 2007; Wu et al., 2013).

Geometrically exact beam theory originated from Euler and Bernoulli's studies on spatial curved rods. Kirchhoff later established static equations for large deformation rods using rigid body dynamics analogies, and the Cosserat brothers subsequently incorporated shear deformation effects. Simo et al. (1995, 1988) extended this framework into a three dimensional dynamic model. This work culminated in a comprehensive theory for the dynamics of geometrically exact beams (Lang and Linn, 2009; Lang et al., 2011), which was systematically documented in seminal works by Antman (2005) and Liu (2006). Unlike lumped-parameter or geometrically inexact beam models, this theory imposes no restrictions on the deformation scale of flexible slender structures, making it ideal for modeling drill string configurations (Alamo and Weber, 2006; Cammarata et al., 2025; Han et al., 2019; Tucker and Wang, 2003; Yang et al., 2025).

Recently, Goicoechea et al. (2019) developed a drill string dynamics model for extended-reach wells on the basis of Cosserat geometrically exact beam theory. Their model integrated wellbore contact, rotational speed, friction, and torque. Solved using COMSOL's weak form interface, it provided an in-depth analysis of stick-slip vibrations during off-bottom rotation. In a subsequent study, Goicoechea et al. (2024a) derived convective equations for the instantaneous cutting depth from rock profile characteristics to compute the WOB and torque. These loads were then coupled as boundary conditions into the geometrically exact beam, enabling a full axial-lateral-torsional vibration simulation. The key findings from this work are as follows: 1) The model captures complex vibrations more accurately, whereas a low-degree-of-freedom model represents severe a simplification. 2) The material damping coefficients in Kelvin-Voigt constitutive models significantly influence stick-slip behavior, suggesting that damping adjustment offers a potential method for vibration suppression. These advances demonstrate the theory's strong potential for modeling the dynamics of drill strings. However, its application to ultra-deep well scenarios remains unexplored, constituting a critical gap for future engineering-focused research.

The authors' previous research employed a scaled-down laboratory apparatus to conduct modeling studies and experimental validations of drill string dynamics based on Cosserat beam theory (Yu et al., 2023). This work systematically analyzed the influence patterns of the inclination angle, rotational speed, WOB, and friction coefficient on drill string lateral vibrations. It also successfully simulated the transition from forward to backward whirling in vertical wells. These findings validate the model's accuracy and establish a foundation for research into full-scale drill string mechanics applications.

This study investigated drill string failure and reduced drilling efficiency caused by severe vibrations in deep drilling operations. Extending prior laboratory experiments and scaled drill string modeling based on Cosserat beam theory, this theoretical framework was applied to ultra-deep 10000 m drill strings. The analysis emphasized the influence of controllable field parameters on lateral vibration behavior, with a focus on previously understudied vibration patterns of potential engineering significance. Key findings were validated against field measurement data. The research objectives are as follows: 1) To apply a geometrically exact beam model for analyzing the dynamic response of ultra-deep drill strings under various parameters and to elucidate the mechanisms governing transitions between lateral vibration modes. 2) To provide theoretically grounded and data-supported methods for vibration control, or to explain existing practical phenomena. 3) To extend the application of Cosserat beam theory to drill string dynamics in ultra-deep wells, thereby enriching the theoretical research methodology in this field.

The structure of this paper is as follows: Section 2 discusses the formulation of the dynamic equations for the model, the setting of distributed constraints, boundary conditions, and initial conditions, and the key parameters for characterizing drill string vibration are defined in subsequent research. Section 3 focuses on engineer-controllable parameters (WOB, rotational speed, and stabilizer size and placement) as primary controlling factors. The influence patterns of these factors on lateral vibration characteristics are analyzed through numerical simulations, new vibration modes are explored, their generation mechanisms are revealed, and corresponding vibration control strategies are proposed. In particular, the effects of rotational speed and WOB on vibration are validated through analysis of wellhead and downhole data. Section 4 summarizes the key conclusions of this research and outlines potential directions for future work.

2. Dynamics modeling

This section outlines the modeling process for drill string dynamics based on Cosserat geometrically exact beam theory, encompassing the formulation of dynamic equations, characterization of distributed loads, and specification of initial and boundary conditions. Beyond the foundational assumptions inherent to Cosserat beam theory, the proposed model incorporates the following supplementary hypotheses:

1) The drill string cross-section is isotropic and initially straight, with joint effects neglected.
2) The wellbore is assumed to be a straight hole with a deviation angle of 0°, and its inner wall is modeled as a uniform cylindrical surface.
3) The friction coefficient within the wellbore is assumed to be spatially uniform.

2.1. Formulation of dynamic equations

A drill string segment of length L is positioned within a straight wellbore OB of radius r_w, as illustrated in Fig. 1(a). An inertial coordinate system O-XYZ is established at the wellhead, where the end face of the drill string at the surface is denoted by P_0, and the end face at the bottom of the well is designated P_L. Considering a cross-section located at an arbitrary position s along the drill string centerline as the subject of analysis, the spatial position of its centroid P is defined by the position vector $\boldsymbol{r}$, which extends from point O to P. At time t, the drill string experiences deformation and motion owing to boundary constraints at both ends and distributed constraints along its length. The distributed internal force and moment between the cross-section at P and its adjacent cross-section are denoted by $\boldsymbol{f}$ and $\boldsymbol{m}$, respectively. On the basis of the beam element assumption, all the dynamic parameters of a given cross-section are defined at its centroid. Accordingly, the internal force and moment are represented by the principal vector $\boldsymbol{F}$ and the principal moment $\boldsymbol{M}$, respectively. During motion, the drill string exhibits a linear velocity vector $\boldsymbol{v}$ and an angular velocity vector $\boldsymbol{\Omega}$. The associated deformations—comprising bending, torsion, shear, and extension—are characterized by the curvature-twist vector $\boldsymbol{\omega}$ (describing bending and torsional deformation) and the strain vector $\boldsymbol{\Gamma}$ (capturing shear and axial deformation), as depicted in Fig. 1(b).

At the centroid P, a principal-axis coordinate system P-xyz is established. The z-axis aligns with the principal axis direction, and the x- and y-axes are orthogonal to the z-axis and lie in the radial directions of the cross-section, as shown in Fig. 1(c). The transformation relationship between the principal-axis coordinate system and the inertial coordinate system is given by:

$$\begin{bmatrix} \boldsymbol{e}_X \\ \boldsymbol{e}_Y \\ \boldsymbol{e}_Z \end{bmatrix} = \begin{bmatrix} q_0^2+q_1^2-q_2^2-q_3^2 & 2(q_1q_2-q_0q_3) & 2(q_1q_3+q_0q_2) \\ 2(q_1q_2+q_0q_3) & q_0^2-q_1^2+q_2^2-q_3^2 & 2(q_2q_3-q_0q_1) \\ 2(q_1q_3-q_0q_2) & 2(q_2q_3+q_0q_1) & q_0^2-q_1^2-q_2^2+q_3^2 \end{bmatrix} \begin{bmatrix} \boldsymbol{e}_x \\ \boldsymbol{e}_y \\ \boldsymbol{e}_z \end{bmatrix} \tag{1}$$

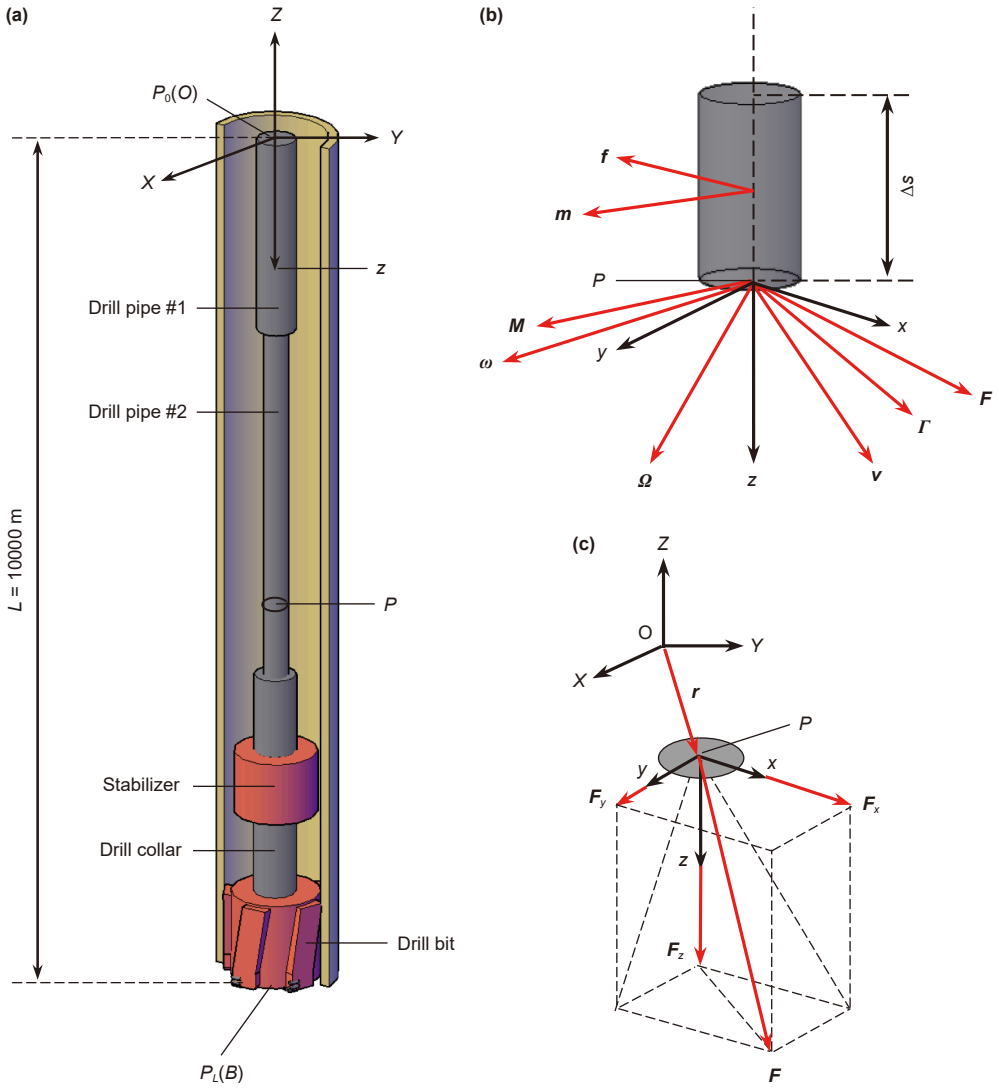

Fig. 1. Dynamic model of an ultra-deep well drill string. (**a**) Drill string configuration and inertial frame *O-XYZ*. (**b**) Principal-axis frame *P-xyz* with dynamic parameters and distributed loads (Δ*s*: element length). (**c**) Coordinate transformation between *P-xyz* and *O-XYZ* showing parameter projections (***F***: principal vector with projections F_x, F_y, F_z).

where $\boldsymbol{e}_X$, $\boldsymbol{e}_Y$, and $\boldsymbol{e}_Z$ are the basis vectors of the inertial coordinate system *O-XYZ*. $\boldsymbol{e}_x$, $\boldsymbol{e}_y$, and $\boldsymbol{e}_z$ are the basis vectors of the principal-axis coordinate system *P-xyz*. q_0, q_1, q_2, and q_3 represent the Euler parameters.

Projecting the vectors within the drill string onto the principal-axis coordinate system yields:

$$\begin{cases} \boldsymbol{F} = F_x\boldsymbol{e}_x + F_y\boldsymbol{e}_y + F_z\boldsymbol{e}_z \\ M = M_x\boldsymbol{e}_x + M_y\boldsymbol{e}_y + M_z\boldsymbol{e}_z \\ \boldsymbol{v} = v_x\boldsymbol{e}_x + v_y\boldsymbol{e}_y + v_z\boldsymbol{e}_z \\ \boldsymbol{\Omega} = \Omega_x\boldsymbol{e}_x + \Omega_y\boldsymbol{e}_y + \Omega_z\boldsymbol{e}_z \\ \boldsymbol{\Gamma} = \Gamma_x\boldsymbol{e}_x + \Gamma_y\boldsymbol{e}_y + \Gamma_z\boldsymbol{e}_z \\ \boldsymbol{\omega} = \omega_x\boldsymbol{e}_x + \omega_y\boldsymbol{e}_y + \omega_z\boldsymbol{e}_z \\ \boldsymbol{f} = f_x\boldsymbol{e}_x + f_y\boldsymbol{e}_y + f_z\boldsymbol{e}_z \\ \boldsymbol{m} = m_x\boldsymbol{e}_x + m_y\boldsymbol{e}_y + m_z\boldsymbol{e}_z \end{cases} \tag{2}$$

where F_x and F_y are shear forces (N). F_z is the axial force (N). M_x and M_y are bending moments (N·m). M_z is torque (N·m). v_x, v_y, and v_z are the linear velocity projections in the principal-axis coordinate system ($m \cdot s^{-1}$). Ω_x, Ω_y, and Ω_z are angular velocity projections ($rad \cdot s^{-1}$). Γ_x, Γ_y, and Γ_z are strain projections. ω_x, ω_y, and ω_z are curvature-twist vector projections ($rad \cdot m^{-1}$). f_x, f_y, and f_z are the projections of the distributed force vector ($N \cdot m^{-1}$). m_x, m_y, and m_z are the projections of the distributed moment vector (N).

The vector $\boldsymbol{r}$ from the origin *O* to the centroid *P* is projected in the inertial coordinate system, yielding:

$$\boldsymbol{r} = X_P\boldsymbol{e}_X + Y_P\boldsymbol{e}_Y + Z_P\boldsymbol{e}_Z \tag{3}$$

where X_P, Y_P, and Z_P represent the coordinates of centroid *P* in the inertial coordinate system (m).

On the basis of Cosserat beam theory, the scalar-form governing equations of drill string dynamics in the principal-axis coordinate system are as follows:

$$\frac{\partial \omega_x}{\partial t} = \frac{\partial \Omega_x}{\partial s} + \omega_y\Omega_z - \omega_z\Omega_y \tag{4a}$$

$$\frac{\partial \omega_y}{\partial t} = \frac{\partial \Omega_y}{\partial s} + \omega_z\Omega_x - \omega_x\Omega_z \tag{4b}$$

$$\frac{\partial \omega_z}{\partial t}=\frac{\partial \Omega_z}{\partial s}+\omega_x\Omega_y-\omega_y\Omega_x \tag{4c}$$

$$\frac{\partial \Gamma_x}{\partial t}=\frac{\partial v_x}{\partial s}+\omega_y v_z-\omega_z v_y-\Omega_y(1+\Gamma_z)+\Omega_z\Gamma_y \tag{4d}$$

$$\frac{\partial \Gamma_y}{\partial t}=\frac{\partial v_y}{\partial s}+\omega_z v_x-\omega_x v_z+\Omega_x(1+\Gamma_z)-\Omega_z\Gamma_x \tag{4e}$$

$$\frac{\partial \Gamma_z}{\partial t}=\frac{\partial v_z}{\partial s}+\omega_x v_y-\omega_y v_x-\Omega_x\Gamma_y+\Omega_y\Gamma_x \tag{4f}$$

$$\rho_s S\frac{\partial v_x}{\partial t}=\frac{\partial F_x}{\partial s}+\omega_y F_z-\omega_z F_y-\rho_s S\left(\Omega_y v_z-\Omega_z v_y\right)+f_x \tag{4g}$$

$$\rho_s S\frac{\partial v_y}{\partial t}=\frac{\partial F_y}{\partial s}+\omega_z F_x-\omega_x F_z-\rho_s S(\Omega_z v_x-\Omega_x v_z)+f_y \tag{4h}$$

$$\rho_s S\frac{\partial v_z}{\partial t}=\frac{\partial F_z}{\partial s}+\omega_x F_y-\omega_y F_x-\rho_s S\left(\Omega_x v_y-\Omega_y v_x\right)+f_z \tag{4i}$$

$$J_x\frac{\partial \Omega_x}{\partial t}=\frac{\partial M_x}{\partial s}+\omega_y M_z-\omega_z M_y+\Gamma_y F_z-(1+\Gamma_z)F_y+\left(J_y-J_z\right)\Omega_y\Omega_z+m_x \tag{4j}$$

$$J_y\frac{\partial \Omega_y}{\partial t}=\frac{\partial M_y}{\partial s}+\omega_z M_x-\omega_x M_z+(1+\Gamma_z)F_x-\Gamma_x F_z+(J_z-J_x)\Omega_z\Omega_x+m_y \tag{4k}$$

$$J_z\frac{\partial \Omega_z}{\partial t}=\frac{\partial M_z}{\partial s}+\omega_x M_y-\omega_y M_x+\Gamma_x F_y-\Gamma_y F_x+\left(J_x-J_y\right)\Omega_x\Omega_y+m_z \tag{4l}$$

$$\frac{\partial q_0}{\partial t}=\frac{1}{2}\left(-q_1\Omega_x-q_2\Omega_y-q_3\Omega_z\right) \tag{4m}$$

$$\frac{\partial q_1}{\partial t}=\frac{1}{2}\left(q_0\Omega_x-q_3\Omega_y+q_2\Omega_z\right) \tag{4n}$$

$$\frac{\partial q_2}{\partial t}=\frac{1}{2}\left(q_3\Omega_x+q_0\Omega_y-q_1\Omega_z\right) \tag{4o}$$

$$\frac{\partial q_3}{\partial t}=\frac{1}{2}\left(-q_2\Omega_x+q_1\Omega_y+q_0\Omega_z\right) \tag{4p}$$

$$\frac{\partial X_P}{\partial t}=\left(q_0^2+q_1^2-q_2^2-q_3^2\right)v_x+2(q_1q_2-q_0q_3)v_y+2(q_1q_3+q_0q_2)v_z \tag{4q}$$

$$\frac{\partial Y_P}{\partial t}=2(q_1q_2+q_0q_3)v_x+\left(q_0^2-q_1^2+q_2^2-q_3^2\right)v_y+2(q_2q_3-q_0q_1)v_z \tag{4r}$$

$$\frac{\partial Z_P}{\partial t}=2(q_1q_3-q_0q_2)v_x+2(q_2q_3+q_0q_1)v_y+\left(q_0^2-q_1^2-q_2^2+q_3^2\right)v_z \tag{4s}$$

Eqs. (4a–4f) are the kinematic equations derived from curved rod kinematics, also referred to as compatibility equations. Eqs. (4g–4i) and (4j–4l) represent the linear momentum and angular momentum equations of elastic rods, respectively, derived from the momentum theorems. In the equations, ρ_s denotes the density of the drill string (kg·m^{-3}). S is the area of the drill string cross-section, m^2. J_x, J_y, and J_z are the per-unit-length moments of inertia about the three axes of the principal-axis coordinate system (kg·m).

Eqs. (4a–4l) represent the general form of the dynamic governing equations derived from Cosserat beam theory, detailed derivations are available in Antman (1998) and Liu (2006). By converting the external loads acting on the drill string into distributed constraints and boundary conditions and incorporating them into this system of equations, the dynamic behavior of the drill string can be comprehensively described. Given that the formulation of certain distributed constraints requires real-time determination of the drill string's spatial configuration, or is more conveniently described in the inertial coordinate system, Eqs. (4m–4s) are introduced into the fundamental equations. Specifically, Eqs. (4m–4p) enable the real-time determination of the Euler parameters at the centroid P of any cross-section of the drill string. These Euler parameters describe the spatial orientation of the cross-section and constitute the direction cosine matrix. Through Eq. (1), the distributed constraints defined in the inertial coordinate system are transformed into the principal-axis coordinate system. These equations are referred to as the attitude equations of the drill string dynamic model. Eqs. (4q–4s) are scalar coordinate equations, and their inclusion in the drill string dynamic equations enables real-time determination of the spatial position of any cross-section.

Antman (1998) introduced a nonlinear constitutive equation for geometrically exact beam on the basis of the Kelvin-Voigt damping model, thereby extending the applicability of this beam model from purely elastic materials to viscoelastic materials. The scalar form of this constitutive equation is given by:

$$\begin{cases} F_x = GS\Gamma_x + 2C_{\dot{\Gamma},x}\dfrac{\partial \Gamma_x}{\partial t} \\ F_y = GS\Gamma_y + 2C_{\dot{\Gamma},y}\dfrac{\partial \Gamma_y}{\partial t} \\ F_z = ES\Gamma_{\boldsymbol{z}} + 2C_{\dot{\Gamma},z}\dfrac{\partial \Gamma_z}{\partial t} \end{cases} \tag{5}$$

$$\begin{cases} M_x = EI_x\omega_x + 2C_{\dot{\mathrm{K}},x}\dfrac{\partial \omega_x}{\partial t} \\ M_y = EI_y\omega_y + 2C_{\dot{\mathrm{K}},y}\dfrac{\partial \omega_y}{\partial t} \\ M_z = GI_z\omega_z + 2C_{\dot{\mathrm{K}},z}\dfrac{\partial \omega_z}{\partial t} \end{cases} \tag{6}$$

In these equations, E and G represent the elastic modulus and shear modulus, respectively (Pa). I_x and I_y are the inertia moments (m^4). I_z is the polar inertia moment (m^4). where $C_{\dot{\mathrm{K}},x}$ and $C_{\dot{\mathrm{K}},y}$ are the material viscous damping coefficients for bending (N·s·m^2). $C_{\dot{\mathrm{K}},z}$ represents the material viscous damping coefficient for torsional (N·s·m^2). $C_{\dot{\Gamma},x}$ and $C_{\dot{\Gamma},y}$ are the material viscous damping coefficients for shear (N·s). $C_{\dot{\Gamma},z}$ is the material viscous damping coefficient for tensile (N·s).

Eqs. (5) and (6) serve as critical components linking the kinematic and dynamic equations of the Cosserat beam theory. When

combined with Eqs. (4a–4s), they ensure that the system has 19 unknowns and an equal number of equations. Furthermore, the viscous damping coefficients of materials and their time derivatives in the constitutive equations significantly influence the whirling motion of the drill string and are often referred to as structural damping coefficients.

2.2. Description of distributed constraints

Distributed constraints refer to uniformly distributed forces or moments acting along the drill string. In this study, the distributed constraints considered include the normal contact force $\boldsymbol{f}_{\mathrm{n}}$, frictional force $\boldsymbol{f}_{\mathrm{f}}$, frictional torque $\boldsymbol{m}_{\mathrm{f}}$, centrifugal force due to rotation $\boldsymbol{f}_{\mathrm{c}}$, buoyed weight $\boldsymbol{f}_{\mathrm{g}}$, and viscous damping moment from the drilling fluid $\boldsymbol{m}_{\mathrm{m}}$. These vector-form distributed constraints are projected onto the principal-axis coordinate system to yield:

$$\begin{cases} \boldsymbol{f}_{\mathrm{n}} = f_{\mathrm{n},x}\boldsymbol{e}_x + f_{\mathrm{n},y}\boldsymbol{e}_y + f_{\mathrm{n},z}\boldsymbol{e}_z \\ \boldsymbol{f}_{\mathrm{f}} = f_{\mathrm{f},x}\boldsymbol{e}_x + f_{\mathrm{f},y}\boldsymbol{e}_y + f_{\mathrm{f},z}\boldsymbol{e}_z \\ \boldsymbol{f}_{\mathrm{c}} = f_{\mathrm{c},x}\boldsymbol{e}_x + f_{\mathrm{c},y}\boldsymbol{e}_y + f_{\mathrm{c},z}\boldsymbol{e}_z \\ \boldsymbol{f}_{\mathrm{g}} = f_{\mathrm{g},x}\boldsymbol{e}_x + f_{\mathrm{g},y}\boldsymbol{e}_y + f_{\mathrm{g},z}\boldsymbol{e}_z \\ \boldsymbol{m}_{\mathrm{f}} = m_{\mathrm{f},x}\boldsymbol{e}_x + m_{\mathrm{f},y}\boldsymbol{e}_y + m_{\mathrm{f},z}\boldsymbol{e}_z \\ \boldsymbol{m}_{\mathrm{m}} = m_{\mathrm{m},x}\boldsymbol{e}_x + m_{\mathrm{m},y}\boldsymbol{e}_y + m_{\mathrm{m},z}\boldsymbol{e}_z \end{cases} \tag{7}$$

where $f_{\mathrm{n},x}$, $f_{\mathrm{n},y}$, and $f_{\mathrm{n},z}$ represent the projections of the normal contact force in the principal-axis coordinate system ($\mathrm{N\cdot m^{-1}}$). $f_{\mathrm{f},x}$, $f_{\mathrm{f},y}$, and $f_{\mathrm{f},z}$ denote the projections of the frictional force ($\mathrm{N\cdot m^{-1}}$). $f_{\mathrm{c},x}$, $f_{\mathrm{c},y}$, and $f_{\mathrm{c},z}$ are the projections of the rotational centrifugal force ($\mathrm{N\cdot m^{-1}}$). $f_{\mathrm{g},x}$, $f_{\mathrm{g},y}$, and $f_{\mathrm{g},z}$ indicate the projections of the linear buoyant weight ($\mathrm{N\cdot m^{-1}}$). $m_{\mathrm{f},x}$, $m_{\mathrm{f},y}$, and $m_{\mathrm{f},z}$ represent the projections of the frictional torque (N). $m_{\mathrm{m},x}$, $m_{\mathrm{m},y}$, and $m_{\mathrm{m},z}$ correspond to the projections of the drilling fluid viscous damping moment (N).

Notably, certain distributed constraints in Eq. (7) can be directly defined along a specific axis of the principal-axis coordinate system, in which case their projections on the remaining two axes are zero. The following discussion addresses each distributed constraint and outlines the formulation process of its scalar forms.

1) Normal contact force

The normal contact force between the drill string and the wellbore wall constrains the motion of the drill string within the borehole boundary. When a relative velocity or a tendency for relative motion arises, this contact simultaneously generates frictional forces. Therefore, the normal contact force must be addressed first. Considering the centroid P of an arbitrary drill string cross-section as the subject of analysis, point A on the wellbore trajectory nearest to point P is defined, as illustrated in Fig. 2(a). For vertical wells, the coordinates of point A can be directly calculated via the perpendicular foot formula from a point to a line, expressed as:

$$\begin{cases} X_A = X_O + c(X_B - X_O) \\ Y_A = Y_O + c(Y_B - Y_O) \\ Z_A = Z_O + c(Z_B - Z_O) \end{cases} \tag{8}$$

where

$$c = \frac{(X_O - X_A)(X_B - X_O) + (Y_O - Y_A)(Y_B - Y_O) + (Z_O - Z_A)(Z_B - Z_O)}{\sqrt{(X_B - X_O)^2 + (Y_B - Y_O)^2 + (Z_B - Z_O)^2}} \tag{9}$$

where X_O, Y_O, and Z_O represent the wellhead coordinates (m). X_B, Y_B, and Z_B denote the bottom hole coordinates (m). X_A, Y_A, and Z_A indicate the coordinates of point A on the trajectory line that is nearest to point P (m).

When the coordinates of point A are known, the distance between points A and P can be further determined as:

$$d_{PA} = \sqrt{(X_A - X_P)^2 + (Y_A - Y_P)^2 + (Z_A - Z_P)^2} \tag{10}$$

where d_{PA} is the distance between point A and point P (m).

The clearance between the drill string and the wellbore is denoted as r_{c}. When the distance d_{PA} is less than r_{c}, there is no contact between the drill string and the wellbore, and the normal contact force is zero. When d_{PA} is greater than or equal to r_{c}, contact occurs between the drill string and the wellbore. By

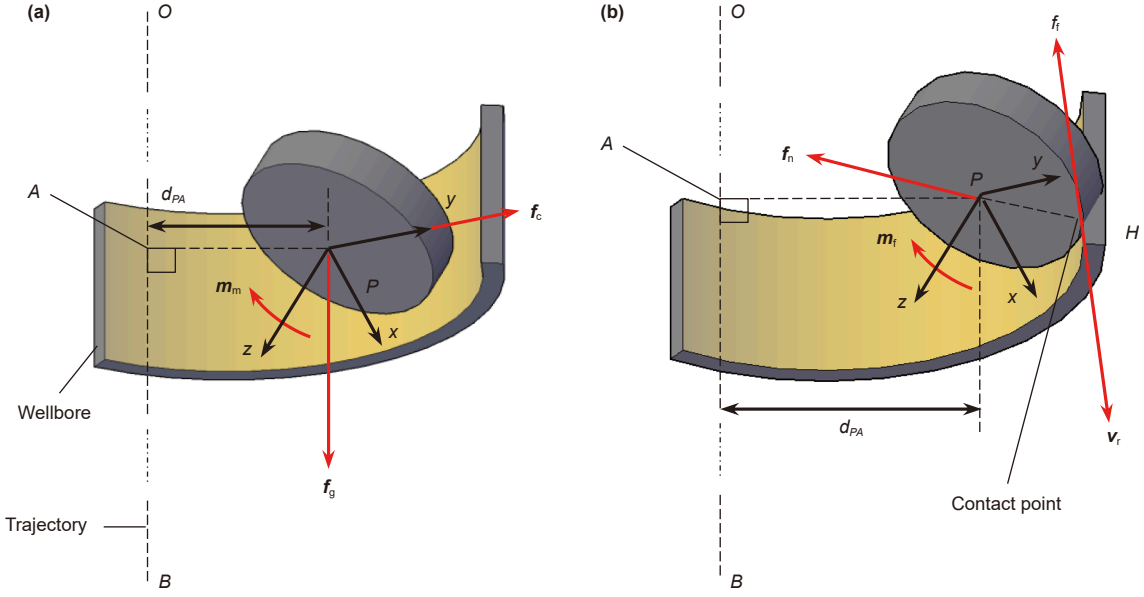

Fig. 2. Distributed constraints. (**a**) Constraints without wellbore contact ($\boldsymbol{f}_{\mathrm{c}}$: centrifugal force, $\boldsymbol{f}_{\mathrm{g}}$: buoyant weight, $\boldsymbol{m}_{\mathrm{m}}$: fluid damping moment). (**b**) Additional contact-induced constraints ($\boldsymbol{f}_{\mathrm{n}}$: normal force, $\boldsymbol{f}_{\mathrm{f}}$: frictional force, $\boldsymbol{m}_{\mathrm{f}}$: frictional torque).

introducing a penalty function and accounting for energy dissipation during the collision process, the projections of the normal contact force in the principal-axis coordinate system are given as:

$$\begin{cases} f_{n,x} = -\left[k_p(d_{PA} - r_c)u_x + k_c v_x\right] \\ f_{n,y} = -\left[k_p(d_{PA} - r_c)u_y + k_c v_y\right] \\ f_{n,z} = -\left[k_p(d_{PA} - r_c)u_z + k_c v_z\right] \end{cases} \tag{11}$$

where

$$\begin{cases} u_x = \dfrac{(q_0^2 + q_1^2 - q_2^2 - q_3^2)(X_P - X_A) + 2(q_1q_2 + q_0q_3)(Y_P - Y_A) + 2(q_1q_3 - q_0q_2)(Z_P - Z_A)}{d_{PA}} \\ u_y = \dfrac{2(q_1q_2 - q_0q_3)(X_P - X_A) + (q_0^2 - q_1^2 + q_2^2 - q_3^2)(Y_P - Y_A) + 2(q_2q_3 + q_0q_1)(Z_P - Z_A)}{d_{PA}} \\ u_z = \dfrac{2(q_1q_3 + q_0q_2)(X_P - X_A) + 2(q_2q_3 - q_0q_1)(Y_P - Y_A) + (q_0^2 - q_1^2 - q_2^2 + q_3^2)(Z_P - Z_A)}{d_{PA}} \end{cases} \tag{12}$$

$$r_c = r_w - r_o \tag{13}$$

where k_p is the wellbore stiffness coefficient ($N\cdot m^{-1}$), k_c is the collision damping coefficient ($N\cdot s\cdot m^{-2}$), and u_x, u_y, and u_z are the projections of the unit vector directed from point A to point P in the principal-axis coordinate system. r_w denotes the wellbore radius (m), and r_o represents the drill string radius (m).

2) Frictional force and torque

Taking the cross-section at point P as an example, the outer side of this section contacts the wellbore at point H at time t, as shown in Fig. 2(b). The scalar form of the relative velocity can be derived from the linear velocity and angular velocity projections in the principal-axis coordinate system as follows:

$$\begin{cases} v_{r,x} = v_x + r_o(\Omega_y u_z - \Omega_z u_y) \\ v_{r,y} = v_y + r_o(\Omega_z u_x - \Omega_x u_z) \\ v_{r,z} = v_z + r_o(\Omega_y u_z - \Omega_z u_y) \end{cases} \tag{14}$$

where $v_{r,x}$, $v_{r,y}$, and $v_{r,z}$ are the projections of the relative velocity vector $\boldsymbol{v}_r$ in the principal-axis coordinate system ($m\cdot s^{-1}$).

The magnitude of the relative velocity vector $\sqrt{v_{r,x}^2 + v_{r,y}^2 + v_{r,z}^2}$ is indicated as $\|v_r\|$. Under ideal conditions, the motion of the drill string along the wellbore can be classified as sliding or rolling on the basis of whether $\|v_r\|$ equals zero, corresponding to kinetic friction or static friction, respectively. However, in numerical computations, it is difficult to precisely satisfy $\|v_r\| = 0$. Therefore, the determination of friction type needs to be relaxed to a certain tolerance range. Now, introducing a relative velocity error limit v_s: when $\|v_r\| > v_s$, the friction type between the drill string and wellbore is kinetic friction. In this case, the kinetic friction force can be expressed as:

$$\begin{cases} f_{f,x} = -\dfrac{\mu_d\sqrt{f_{n,x}^2 + f_{n,y}^2 + f_{n,z}^2}v_{r,x}}{\|v_r\|} \\ f_{f,y} = -\dfrac{\mu_d\sqrt{f_{n,x}^2 + f_{n,y}^2 + f_{n,z}^2}v_{r,y}}{\|v_r\|} \\ f_{f,z} = -\dfrac{\mu_d\sqrt{f_{n,x}^2 + f_{n,y}^2 + f_{n,z}^2}v_{r,z}}{\|v_r\|} \end{cases} \tag{15}$$

where μ_d is the coefficient of kinetic friction.

The frictional torque can be further determined from the kinetic friction force:

$$\begin{cases} m_{f,x} = r_o\left(f_{f,y}u_z - f_{f,z}u_y\right) \\ m_{f,y} = r_o\left(f_{f,z}u_x - f_{f,x}u_z\right) \\ m_{f,z} = r_o\left(f_{f,x}u_y - f_{f,y}u_x\right) \end{cases} \tag{16}$$

When $|v_r| \le v_s$, the friction between the drill string and wellbore may transition to static friction, necessitating additional verification. In the case of the cross-section containing point P, which is in contact with the wellbore under rolling conditions, setting the relative velocity projections in Eq. (14) to zero and computing their partial derivatives with respect to t yields the governing equations. By omitting negligible terms $\partial X_A/\partial t$, $\partial Y_A/\partial t$, and $\partial Z_A/\partial t$ while enforcing the distance parameter d_{PA} equal to the clearance between the drill string and wellbore r_c, the following simplified formulation is obtained:

$$\begin{cases} \dfrac{\partial v_x}{\partial t} + r_o\left(\dfrac{\partial \Omega_y}{\partial t}u_z - \dfrac{\partial \Omega_z}{\partial t}u_y\right) = \dfrac{r_o}{r_c}(\Omega_y v_z - \Omega_z v_y) \\ \dfrac{\partial v_y}{\partial t} + r_o\left(\dfrac{\partial \Omega_z}{\partial t}u_x - \dfrac{\partial \Omega_x}{\partial t}u_z\right) = \dfrac{r_o}{r_c}(\Omega_z v_x - \Omega_x v_z) \\ \dfrac{\partial v_z}{\partial t} + r_o\left(\dfrac{\partial \Omega_y}{\partial t}u_z - \dfrac{\partial \Omega_z}{\partial t}u_y\right) = \dfrac{r_o}{r_c}(\Omega_y v_z - \Omega_z v_y) \end{cases} \tag{17}$$

By combining Eqs. (4g–4l), (16), and (17), where the linear acceleration projections are denoted as $\dot{v}_x$, $\dot{v}_y$, and $\dot{v}_z$, the angular acceleration projections as $\dot{\Omega}_x$, $\dot{\Omega}_y$, and $\dot{\Omega}_z$, and the static friction projections as $f_{s,x}$, $f_{s,y}$, and $f_{s,z}$, a coupled system of equations can be established.

The static friction forces, linear accelerations, and angular accelerations are treated as unknown parameters and placed on the

left-hand side of the equations, whereas all currently known parameters—including all distributed forces and moments except static friction forces and friction torques—are positioned on the right-hand side. The resulting system of simultaneous equations can be expressed as:

$$\begin{bmatrix} \rho_s S & 0 & 0 & -1 & 0 & 0 & 0 & 0 & 0 \\ 0 & \rho_s S & 0 & 0 & -1 & 0 & 0 & 0 & 0 \\ 0 & 0 & \rho_s S & 0 & 0 & -1 & 0 & 0 & 0 \\ 0 & 0 & 0 & 0 & r_o u_z & -r_o u_y & J_x & 0 & 0 \\ 0 & 0 & 0 & -r_o u_z & 0 & r_o u_x & 0 & J_y & 0 \\ 0 & 0 & 0 & r_o u_y & -r_o u_x & 0 & 0 & 0 & J_z \\ 1 & 0 & 0 & 0 & 0 & 0 & 0 & r_o u_z & -r_o u_y \\ 0 & 1 & 0 & 0 & 0 & 0 & -r_o u_z & 0 & r_o u_x \\ 0 & 0 & 1 & 0 & 0 & 0 & r_o u_y & -r_o u_x & 0 \end{bmatrix} \begin{bmatrix} \dot{v}_x \\ \dot{v}_y \\ \dot{v}_z \\ f_{s,x} \\ f_{s,y} \\ f_{s,z} \\ \dot{\Omega}_x \\ \dot{\Omega}_y \\ \dot{\Omega}_z \end{bmatrix} = \begin{bmatrix} k_1 \\ k_2 \\ k_3 \\ k_4 \\ k_5 \\ k_6 \\ k_7 \\ k_8 \\ k_9 \end{bmatrix} \tag{18}$$

where k_1–k_9 represent the sums of the terms on the right-hand sides of Eqs. (4g–4l) and (17), respectively.

Take the inverse of the coefficient matrix in Eq. (18) and obtain the static friction forces $f_{s,x}$, $f_{s,y}$, and $f_{s,z}$ through matrix operations. The magnitude of the static friction force $\sqrt{f_{s,x}^2+f_{s,y}^2+f_{s,z}^2}$ is denoted as $\|f_s\|$, and the magnitude of the normal contact force $\sqrt{f_{n,x}^2+f_{n,y}^2+f_{n,z}^2}$ is denoted as $\|f_n\|$. If $\|f_s\| \le \mu_d\|f_n\|$, the static friction assumption holds, yielding $f_{f,x}=f_{s,x}$, $f_{f,y}=f_{s,y}$, and $f_{f,z}=f_{s,z}$. If $\|f_s\| > \mu_d\|f_n\|$, the magnitude of the frictional force still satisfies Coulomb's friction law, but its direction is determined by the static friction force. In this case, Eq. (15) should be modified as:

$$\begin{cases} f_{f,x} = \mu_d\|f_n\|\dfrac{f_{s,x}}{\|f_s\|} \\ f_{f,y} = \mu_d\|f_n\|\dfrac{f_{s,y}}{\|f_s\|} \\ f_{f,z} = \mu_d\|f_n\|\dfrac{f_{s,z}}{\|f_s\|} \end{cases} \tag{19}$$

3) Centrifugal force

Mass imbalance is the primary cause of lateral vibrations in drill strings, and this factor must be incorporated into the drill string system when analyzing such vibrations. Taking the cross-section at point P as an example, assume that a concentrated mass point G is located at a fixed position within this section. The distance between point G and point P is defined as the eccentricity, denoted by e. Since point G and the x- and y-axes of the principal-axis coordinate system are fixed within the cross-section—implying that the relative positions of the mass point and the coordinate axes remain unchanged during rotation—point G is placed directly on the y-axis. When a rotational speed is applied along the z-axis, the centrifugal force arising from mass eccentricity can be expressed as:

$$f_{c,y} = \rho_s S e \Omega_z^2 \tag{20}$$

The centrifugal force due to rotation acts from the geometric center of the cross-section toward the mass center and is directly established in the non-inertial reference frame. Consequently, there is no need to consider additional moments and Coriolis forces.

4) Buoyed weight

Taking the cross section at point P as an example, the gravitational force vector in the inertial coordinate system is expressed as $-\rho_s S\boldsymbol{e}_Z$. Eq. (1) is used to transform it into the principal-axis coordinate system while considering the buoyancy of the drilling fluid, and the scalar form of the buoyant weight can be obtained as:

$$\begin{cases} f_{g,x} = -2\left(1-\dfrac{p_m}{p_s}\right)(q_1q_3 - q_0q_2)\rho_s S \\ f_{g,y} = -2\left(1-\dfrac{p_m}{p_s}\right)(q_2q_3 + q_0q_1)\rho_s S \\ f_{g,z} = -\left(1-\dfrac{p_m}{p_s}\right)\left(q_0^2 - q_1^2 - q_2^2 + q_3^2\right)\rho_s S \end{cases} \tag{21}$$

where ρ_m represents the density of the drilling fluid ($kg\cdot m^{-3}$).

5) Drilling fluid viscous damping

This study considers only the viscous damping moment of the drilling fluid in the torsional direction, employing a torque calculation formula proposed by Bourgoyne et al. (1986) for plastic fluids acting on the outer surface of the drill string, which is specifically expressed as:

$$m_{m,z} = -2\pi\tau {r_o}^2 \tag{22}$$

where

$$\tau = \tau_0 + \mu_p\gamma \tag{23}$$

$$\gamma = \frac{\Omega_z}{r_o^2\left(\frac{1}{r_o^2}-\frac{1}{r_w^2}\right)} \tag{24}$$

where $m_{m,z}$ represents the viscous damping moment along the z-axis of the principal-axis coordinate system (N), τ denotes the shear stress of the drilling fluid (N·s), τ_0 represents the yield point (Pa), μ_p indicates the plastic viscosity (Pa·s), and γ represents the shear rate ($rad\cdot s^{-1}$).

The distributed forces and moments mentioned above are summed over the three principal axis directions, yielding:

$$\begin{cases} f_x = f_{\mathrm{n},x} + f_{\mathrm{f},x} + f_{\mathrm{g},x} \\ f_y = f_{\mathrm{n},y} + f_{\mathrm{f},y} + f_{\mathrm{g},y} + f_{\mathrm{c},y} \\ f_z = f_{\mathrm{n},z} + f_{\mathrm{f},z} + f_{\mathrm{g},z} \end{cases} \tag{25}$$

$$\begin{cases} m_x = m_{\mathrm{f},x} \\ m_y = m_{\mathrm{f},y} \\ m_z = m_{\mathrm{f},z} + m_{\mathrm{m},z} \end{cases} \tag{26}$$

By substituting Eqs. (25) and (26) into Eqs. (4g–4l), the system of drill string dynamics equations can be fully formulated.

2.3. Establishment of boundary and initial conditions

The boundary condition for the drill string configuration in Fig. 1 is established by defining a principal-axis coordinate system P_0-xyz at the centroid of the P_0 end section. The resultant external moment $\boldsymbol{M}_0$, resultant external force $\boldsymbol{F}_0$, angular velocity $\boldsymbol{\Omega}_0$, and linear velocity $\boldsymbol{v}_0$ acting on the end face are spatially resolved into projections along the axes of this coordinate system:

$$\begin{cases} \boldsymbol{M}_0 = M_{0,x}\boldsymbol{e}_x + M_{0,y}\boldsymbol{e}_y + M_{0,z}\boldsymbol{e}_z \\ \boldsymbol{F}_0 = F_{0,x}\boldsymbol{e}_x + F_{0,y}\boldsymbol{e}_y + F_{0,z}\boldsymbol{e}_z \\ \boldsymbol{\Omega}_0 = \Omega_{0,x}\boldsymbol{e}_x + \Omega_{0,y}\boldsymbol{e}_y + \Omega_{0,z}\boldsymbol{e}_z \\ \boldsymbol{v}_0 = v_{0,x}\boldsymbol{e}_x + v_{0,y}\boldsymbol{e}_y + v_{0,z}\boldsymbol{e}_z \end{cases} \tag{27}$$

where $M_{0,x}$, $M_{0,y}$, and $M_{0,z}$ represent the projections of the resultant external moment $\boldsymbol{M}_0$ in the principal-axis coordinate system (N·m). $F_{0,x}$, $F_{0,y}$, and $F_{0,z}$ denote the projections of the resultant external force $\boldsymbol{F}_0$ (N). $\Omega_{0,x}$, $\Omega_{0,y}$, and $\Omega_{0,z}$ correspond to the angular velocity projections of $\boldsymbol{\Omega}_0$ (rad·s^{-1}). $v_{0,x}$, $v_{0,y}$, and $v_{0,z}$ describe the linear velocity projections of $\boldsymbol{v}_0$ (m·s^{-1}).

The P_0 end, fixed at the origin O, is considered a special type of three-dimensional fixed support, as illustrated in Fig. 3(a). The position of the P_0 end remains stationary at all times, with $v_{0,x}$, $v_{0,y}$, and $v_{0,z}$ equal to zero. This end is permitted to rotate only about the z-axis of the principal-axis coordinate system, resulting in $\Omega_{0,x}$ and $\Omega_{0,y}$ being zero. The angular velocity $\Omega_{0,z}$ and torque $M_{0,z}$ can simultaneously exist along the z-axis, representing the rotational speed and torque, respectively. However, $\Omega_{0,z}$ and $M_{0,z}$ are mutually exclusive parameters, meaning that only one of them can be specified as a known condition—typically, the angular velocity $\Omega_{0,z}$ is provided. Consequently, the determinable parameters at the P_0 end include $v_{0,x}$, $v_{0,y}$, $v_{0,z}$, $M_{0,x}$, $M_{0,y}$, and $\Omega_{0,z}$.

The drill bit crown end P_L, located at bottom hole B, is modeled as a special three-dimensional sliding hinge support, as shown in Fig. 3(b). A principal-axis coordinate system P_L-xyz is established at the centroid of the P_L end, where the external principal moment $\boldsymbol{M}_L$, external principal force $\boldsymbol{F}_L$, angular velocity $\boldsymbol{\Omega}_L$, and linear velocity $\boldsymbol{v}_L$ can be projected into this coordinate system in accordance with Eq. (27). When a full-gauge bit is assumed, the centroid of the P_L end coincides with the borehole center. In contrast to the P_0 end, the P_L end is permitted to move along the z-axis, reflecting the axial advancement of the bit along the well trajectory, which results in $v_{L,x}$ and $v_{L,y}$ being zero. Additionally, the determinable parameters at the P_L end include the axial force $F_{L,z}$, which represents the WOB, and the torque $M_{L,z}$, which represents the bit's reactive torque (TOB). Importantly, $F_{L,z}$ and the axial velocity $v_{L,z}$ are mutually exclusive; since WOB is more readily measurable, $F_{L,z}$ is typically specified as the known boundary condition. Consequently, the parameters that can be determined at the P_L end are $v_{L,x}$, $v_{L,y}$, $M_{L,x}$, $M_{L,y}$, $M_{L,z}$, and $F_{L,z}$.

By applying the constitutive equations to convert the known external forces and moments at both end faces into strain and bending–torsional deformations, the boundary conditions for the drill string dynamic model are defined as follows:

$$\begin{cases} \Omega_{0,x} = \Omega_{0,y} = 0 \\ \Omega_{0,z} = \Omega_0 \\ v_{0,x} = v_{0,y} = v_{0,z} = 0 \\ \omega_{\mathrm{L},x} = \omega_{\mathrm{L},y} = 0 \\ \omega_{\mathrm{L},z} = -\dfrac{T_{\mathrm{b}}}{GI_z} \\ v_{\mathrm{L},x} = v_{\mathrm{L},y} = 0 \\ \Gamma_{\mathrm{L},z} = -\dfrac{W_{\mathrm{b}}}{ES} \end{cases} \tag{28}$$

where $\omega_{0,x}$ and $\omega_{0,y}$ are the projections of the curvature-twist vector at the P_0 end (rad·m^{-1}), Ω_0 is the fixed rotational speed at the P_0 end (rad·s^{-1}), $\omega_{L,x}$, $\omega_{L,y}$, and $\omega_{L,z}$ are the projections of the curvature-twist vector at the P_L end (rad·m^{-1}), and $\Gamma_{L,z}$ is the tensile strain at the P_L end.

Assuming that the drill string is initially stationary at the center of a straight borehole, with its central axis coinciding with the borehole trajectory, the coordinates X_P, Y_P, and Z_P of the centroid of any cross-section correspond to the trajectory coordinates at the corresponding depth (0, 0, $-Z_A(s)$). A finite difference scheme is constructed for $\partial F_z/\partial s = -f_{g,z}$ to obtain the axial force $F_z(s)$ at different borehole depths, and the constitutive equations are then used to determine the axial strain $\Gamma_z(s)$. By converting the direction cosine matrix—defined by the inclination and azimuth angles—into Euler parameters through the quaternion extraction method, the Euler parameters $q_0(s)$, $q_1(s)$, $q_2(s)$, and $q_3(s)$ at any cross-section can be determined. With the exception of the coordinates, axial strain, and Euler parameters, all other parameters are initialized to zero. The initial conditions are formulated as:

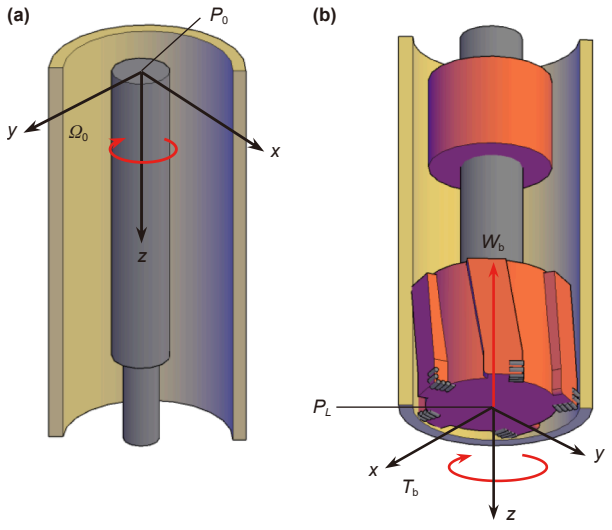

Fig. 3. Boundary condition settings. (**a**) P_0 end of the drill string at the wellhead, where Ω_0 represents the rotary table speed. (**b**) P_L end of the drill bit crown at the bottom hole, with T_b denoting the bit reactive torque and W_b indicating the WOB.

$$\begin{cases} v_X(s,t_0)=v_Y(s,t_0)=v_Z(s,t_0)=0 \\ \Omega_X(s,t_0)=\Omega_Y(s,t_0)=\Omega_Z(s,t_0)=0 \\ \omega_X(s,t_0)=\omega_Y(s,t_0)=\omega_Z(s,t_0)=0 \\ \Gamma_X(s,t_0)=\Gamma_Y(s,t_0)=0 \\ \Gamma_Z(s,t_0)=\Gamma_Z(s) \\ q_0(s,t_0)=q_0(s) \\ q_1(s,t_0)=q_1(s) \\ q_2(s,t_0)=q_2(s) \\ q_3(s,t_0)=q_3(s) \\ X_P(s,t_0)=Y_P(s,t_0)=0 \\ Z_P(s,t_0)=-Z_A(s) \end{cases} \tag{29}$$

After incorporating the boundary condition Eq. (28) and initial condition Eq. (29) into the drill string dynamics Eq. (4), the system of equations becomes closed. For the numerical solution of this equation system, reference methods include the finite element weak form and the finite difference method. Importantly, the finite difference scheme is not unique (Armero, 2025). Previous research has proposed a numerical solution approach that uses 4th–5th order Runge-Kutta integration for temporal derivatives and 2nd-order central differencing for spatial derivatives (Yu et al., 2023). The study also validated the model through a scaled experimental setup capable of simulating the motion states of the BHA under various inclination angles, rotational speeds, WOB, and friction coefficients, thereby demonstrating the accuracy and rationality of the model. Additional details regarding the experimental apparatus can be found in the referenced work (Li et al., 2020).

2.4. Development of evaluation metrics

After the drill string dynamics model are established, the dynamic parameters at any cross-section of the drill string at different times can be obtained, including all the projections, coordinates, and Euler parameters defined in Eq. (2). The use of these parameters and their combinations to characterize the dynamic behavior of the full-wellbore drill string comprehensively provides the foundation for subsequent lateral vibration analysis. Given that variations in drill string dimensions result in differing wellbore clearances at various depths, the maximum amplitude of lateral vibrations also varies accordingly. To quantify the extent of deviation of the drill string's centroid from the wellbore center, a lateral deviation ratio R is introduced. Taking the cross-section at point P as an example, the lateral deviation ratio is calculated as follows:

$$R=\frac{\sqrt{(X_A-X_P)^2+(Y_A-Y_P)^2}}{r_c} \tag{30}$$

In addition to the lateral deviation ratio R, the tangential velocity v_t can be used to characterize the revolution speed and direction of lateral vibrations and is also referred to as the revolution linear velocity. The expression is formulated as follows:

$$v_t=\frac{(Y_A-Y_P)v_X-(X_A-X_P)v_Y}{d_{PA}} \tag{31}$$

where

$$\begin{cases} v_X=\left(q_0^2+q_1^2-q_2^2-q_3^2\right)v_X+2(q_1q_2-q_0q_3)v_Y+2(q_1q_3+q_0q_2)v_Z \\ v_Y=2(q_1q_2+q_0q_3)v_X+\left(q_0^2-q_1^2+q_2^2-q_3^2\right)v_Y+2(q_2q_3-q_0q_1)v_Z \end{cases} \tag{32}$$

where v_X and v_Y are the linear velocity projections in the inertial coordinate system ($m\cdot s^{-1}$). When $v_t>0$, the cross-section at point P undergoes backward revolution. When $v_t<0$, it undergoes forward revolution.

The lateral acceleration at point P is expressed as follows:

$$a_r=\sqrt{\left(\frac{\partial v_X}{\partial t}\right)^2+\left(\frac{\partial v_Y}{\partial t}\right)^2} \tag{33}$$

where a_r represents the lateral acceleration at the centroid ($m\cdot s^{-2}$).

This study proposes identifying the motion states of the drill string through the lateral deviation ratio R and revolution linear velocity v_t while adopting the lateral acceleration a_r to quantify the severity of vibrations. Furthermore, WOB is one of the primary factors influencing lateral vibrations. As the WOB increases, the drill string may undergo buckling, resulting in more complex dynamic behaviors. Therefore, the bending stress σ_b is used to characterize the potential damage caused by vibrations to the drill string. The bending stress is calculated as follows:

$$\sigma_b=E\sqrt{\left(\omega_x^2+\omega_y^2\right)}r_o \tag{34}$$

3. Calculation and analysis

On the basis of Cosserat beam theory, dynamic modeling is performed for the entire drill string in a 10000 m ultra-deep well. Through this model, lateral vibrations under different key controlling factors are simulated and analyzed, and effective vibration control strategies are subsequently proposed.

3.1. Research methodology

To systematically characterize the lateral vibrations of drill strings in ultra-deep wells under varying conditions, this study adopts a progressive complexity modeling and analysis approach. The methodology involves incrementally introducing downhole components to a base drill pipe configuration and evaluating their influence on the dynamic behavior of each resulting assembly. The specific research rationale and workflow are outlined as follows:

1) Uniform drill pipe configuration. The drill string is initially modeled via drill pipes of identical dimensions throughout its length. Although deploying an entire drill string composed solely of uniform drill pipes is impractical in real drilling operations owing to safety and structural concerns, this simplified model illustrates fundamental drill string behavior under helical buckling, thereby establishing a baseline for subsequent, more complex simulations.
2) Heterogeneous drill string assembly. In this stage, the upper and lower segments of the drill string are replaced with larger-diameter drill pipes and higher-stiffness components, such as drill collars or heavyweight drill pipes. This configuration facilitates the analysis of vibration responses under varying rotational speeds and WOB, enabling more realistic simulations of actual drilling.
3) Stabilizer-integrated BHA. Stabilizers are incorporated into the BHA. The annular clearance between the drill string and wellbore is a critical factor influencing lateral vibrations. Installing stabilizers with larger outer diameters to adjust this clearance allows for a systematic investigation of its impact on ultra-deep well vibration characteristics. Furthermore, trajectory control in deep formations remains a major challenge. Owing to the limited high-temperature tolerance of active anti-deviation tools (e.g., vertical drilling systems and positive displacement

Table 1
Computational parameters required for the dynamic model.

Parameters	Value	Parameters	Value
Wellbore diameter d_w	0.2413 m	Bit reactive torque T_b	3000 N·m
Drill string total length L	10000 m	Drilling fluid yield point τ_0	10 Pa
Eccentricity of drill pipe e	$0.003r_o$ m	Kinetic friction coefficient μ_d	0.2
Eccentricity of BHA e	$0.013r_o$ m	Drilling fluid density ρ_m	1300 kg·m^{-3}
Drill string density ρ_s	7850 kg·m^{-3}	Drilling fluid plastic viscosity μ_p	0.038 Pa·s
Elastic modulus E	2.10×10^{11} Pa	Collision damping coefficient k_c	60 N·s·m^{-2}
Shear modulus G	7.84×10^{10} Pa	Wellbore stiffness coefficient k_p	10^8 N·m^{-1}
Bending materials viscous damping coefficient $C_{K,x}$ and $C_{K,y}$	6300 N·s·m^2	Torsional materials viscous damping coefficient $C_{K,z}$	4850 N·s·m^2
Shear materials viscous damping coefficient $C_{\Gamma,x}$ and $C_{\Gamma,y}$	7000 N·s	Tensile materials viscous damping coefficient $C_{\Gamma,z}$	18800 N·s

motors), field operations often rely on passive pendulum BHAs for deviation control. To ensure the effectiveness of the pendulum effect, the number and placement of stabilizers must strictly adhere to standardized pendulum BHA design criteria.

The key parameters beyond the WOB, rotational speed, and drill string dimensions are listed in Table 1. Notably, certain parameters—such as the mass eccentricity of the drill string, material viscous damping coefficient, and friction coefficient—are difficult to measure accurately in practice. These values are typically estimated through empirical methods or calibrated against extensive simulations. While such estimations may introduce discrepancies between simulated results and actual field data, the overall behavioral trends remain consistent. Therefore, qualitative analyses derived from these simulations are highly valuable for practical engineering.

3.2. Vibration characteristics under buckling

Based on the research methodology outlined in Section 3.1 and the parameters of the model listed in Table 1, and assuming that the entire drill string consists of drill pipes with an outer diameter of 0.127 m and an inner diameter of 0.109 m, the dynamic characteristics under a rotational speed of 40 rpm and a WOB of 50 kN are presented in Fig. 4. The lateral deviation rate R and bending stress σ_b of the drill string below the neutral point remained at their peak levels within 150 s, indicating continuous contact between the lower drill string and the wellbore, along with significant bending deformation. For the drill pipe located 10 m above the bit (where the bending stress reaches its maximum), the lateral displacement of its centroid in the inertial coordinate system was analyzed using energy spectral density (ESD). The time-domain signal amplitudes in both the X- and Y- axes are equal to the clearance between the drill pipe and wellbore ±0.0571 m. Given that both axes exhibit identical vibration characteristics (see Fig. 5(a)), their frequency-domain signals are also identical. Using the Y-axis ESD as an example, the dominant modal frequency is 0.033 Hz, indicating that the drill pipe undergoes periodic revolution along the wellbore wall within a period of 30 s (see Fig. 5(b)).

When the motion trajectory of the drill string illustrated in Fig. 6 is further integrated, the portion of the drill string below the neutral point clearly exhibits three-dimensional helical deformation accompanied by backward revolution. Considering the relationship between the backward whirling frequency and rotational speed, under the given operational conditions of 40 rpm and a wellbore clearance of 0.057 m, the theoretical rolling backward whirling period is approximately 1.35 s. This suggests that the observed motion deviates from typical backward whirling behavior. By utilizing the buckling load equations established by Lubinski (1950) and Cebeci et al. (2019), the critical helical buckling load for a rotating drill pipe with a diameter of 0.127 m is determined to be 15.5 kN. Thus, the current deformation pattern is identified as quasi-static helical buckling. Despite the low lateral acceleration and slow revolution linear velocity, the drill string experiences considerable bending stress, averaging 16.7 MPa. Moreover, this buckled state reduces the efficiency of axial force and torque transmission and compromises trajectory control stability (Huang et al., 2016).

3.3. Effect of rotational speed

By replacing both the upper and lower drill pipes with larger-diameter drill pipes and higher-stiffness drill collars,

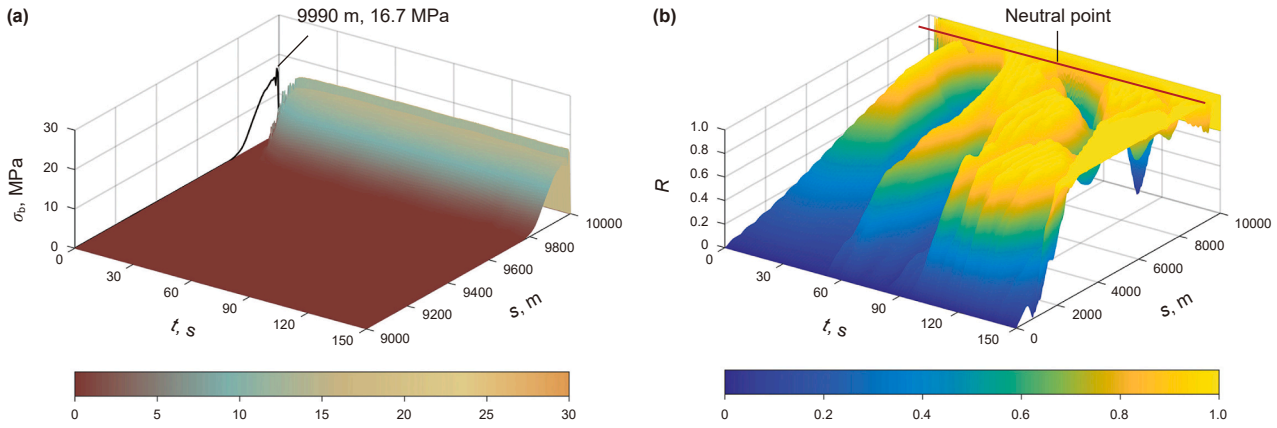

Fig. 4. Dynamic characteristics of the full-length drill pipe at 40 rpm and 50 kN. (**a**) Bending stress. (**b**) Lateral deviation ratio.

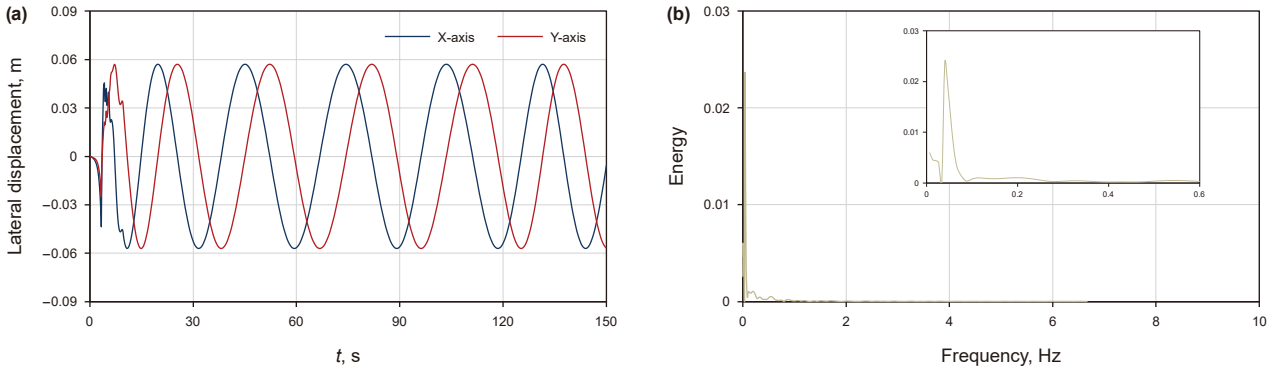

Fig. 5. Lateral displacement time-domain signal of the drill pipe centroid at 10 m above the bit and the corresponding energy spectral density. (**a**) Time-domain signal of lateral displacement. (**b**) ESD along the *Y*-axis.

respectively, the specifications of the drill string within the BHA are updated as shown in Table 2. Under a constant WOB of 50 kN, the evolution of the entire drill string dynamic characteristics along the wellbore, as the rotational speed increases from 40 to 100 rpm, is depicted in Fig. 7.

On the basis of the analysis results in Fig. 7, the drill collar remains the component most susceptible to severe lateral vibrations, owing to axial compression and greater eccentricity. Its revolution linear velocity exhibits repeated intermittent nonnegative peaks over time, accompanied by noticeable fluctuations in the lateral acceleration at these instants. Fig. 8(a) and (b) show the lateral displacement of the drill collar centroid at 10 m above the bit and its relative velocity under a rotational speed of 100 rpm, respectively. An analysis of Figs. 7(d) and 8 indicates that the peaks in the revolution linear velocity coincide with high-frequency lateral displacements and near-zero relative velocities, suggesting that the drill collar enters a state of pure rolling backward whirling during these intervals. At other times, it exhibits low-frequency backward revolution or irregularly alternates between forward and backward motion. Furthermore, as the rotational speed increases, the frequency of peaks in the revolution linear velocity also increases, indicating that higher rotational speeds more frequently induce pure rolling backward whirling in the drill collar. This aligns with the established understanding of the effect of rotational speed on lateral vibration modes (Zhang et al., 2023a). Notably, when the drill collar enters a state of pure rolling backward whirling, the bending stress increases sharply (see Fig. 9), which substantially increasing the risk of drill string wear and fatigue failure.

Table 2
Material and geometric parameters and unit lengths of drill string components in the BHA.

Drill string	Length, m	Outer diameter, m	Inner diameter, m
Drill pipe #1	6800	0.1492	0.127
Drill pipe #2	2980	0.1270	0.109
Drill collar	220	0.1778	0.0714
Drill bit	0.25	0.2413	–

Assuming a vertical wellbore, the upper section of the tensioned drill pipe experiences lateral vibration characterized by intermittent contact with the wellbore wall. As the rotational speed increases, the lateral displacement rate R deviates from a linear trend (see Fig. 10), primarily because of the superposition of lateral vibrations propagating along the drill string. Centrifugal forces resulting from mass eccentricity and drill string rotation amplify lateral vibrations at relatively high rotational speeds. Moreover, high- and low-frequency alternating vibrations near the drill collar propagate upward as transverse waves. This mechanism is supported by the trends in the revolution linear velocity over time and depth across different rotational speed ranges, as shown in Fig. 7((a-1)–(d-1)). The interaction of these waves disturbs the vibration patterns of the drill pipe, thereby increasing the complexity of the vibrational modes.

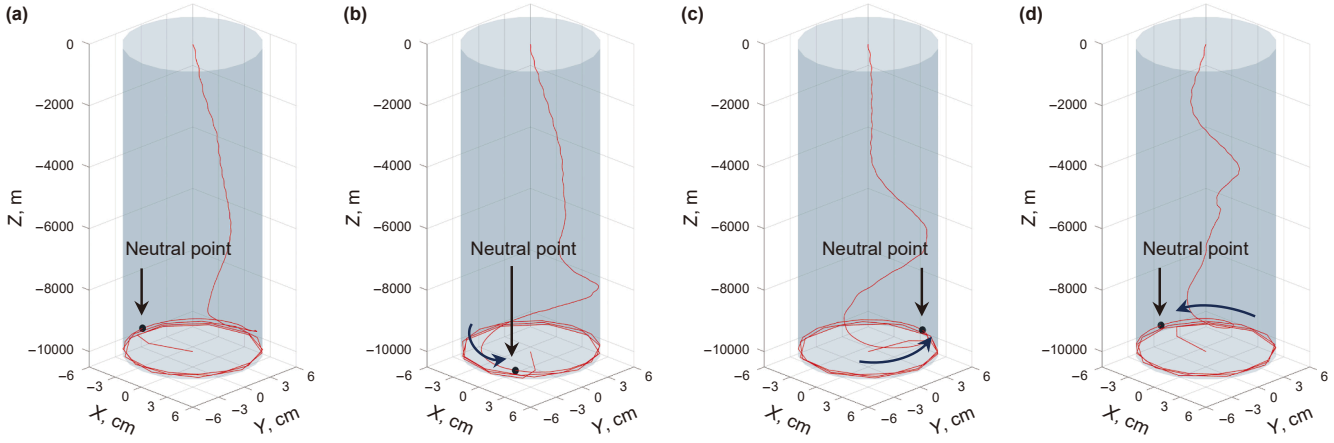

Fig. 6. Motion state of the drill string during one revolution cycle at 40 rpm and 50 kN. (**a**–**d**) Lateral vibration of the drill string at 60, 70, 80 and 90 s, respectively. The transparent blue cylinder represents the clearance between the drill string and the wellbore wall. The red solid line indicates the centerline of the drill pipe. The blue arrow shows the direction of motion of the drill string. The black solid circle marks the current position of the neutral point.

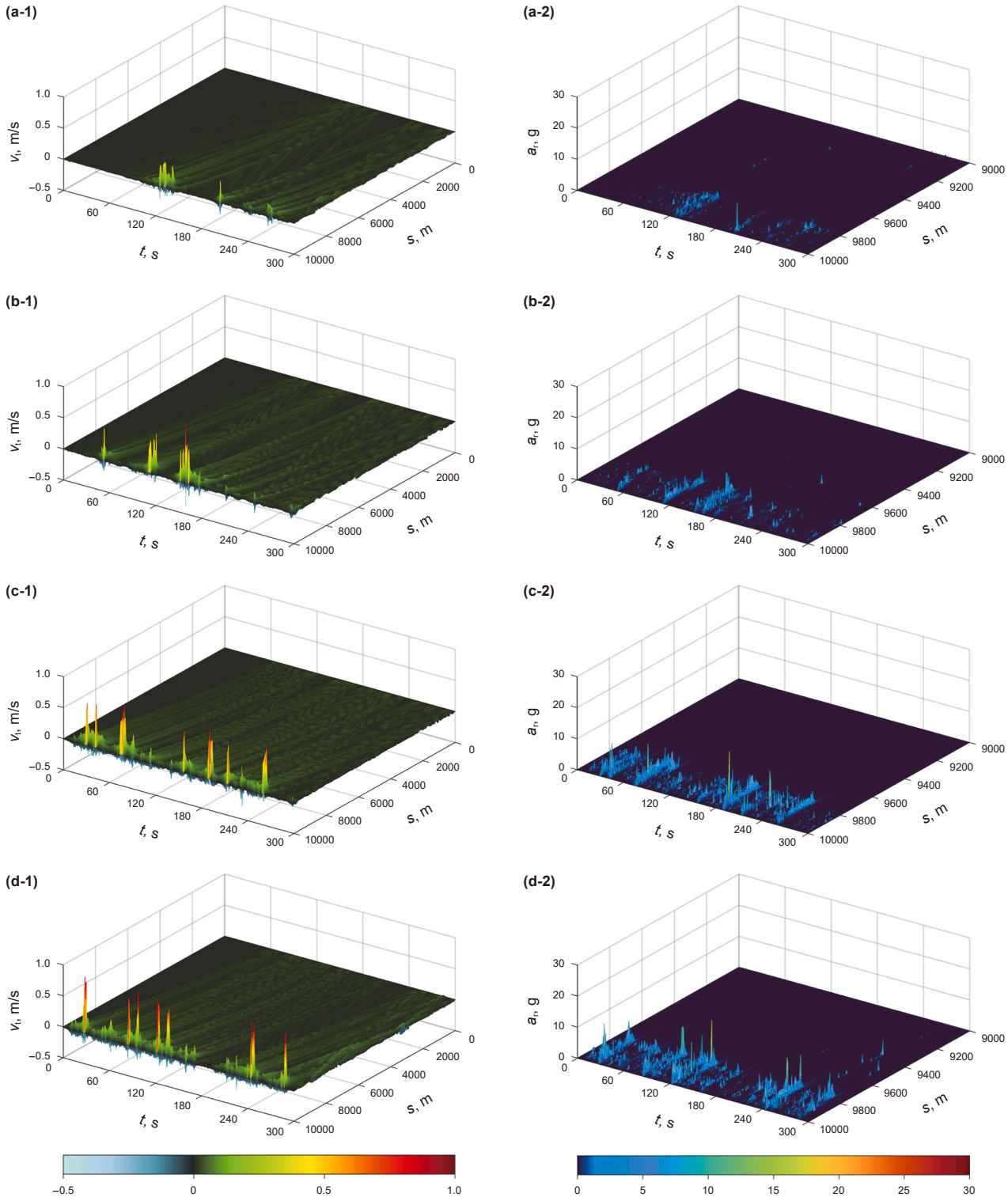

Fig. 7. Evolution of drill string dynamic characteristics with increasing rotational speed under a WOB of 50 kN. Subplots (**a-1**) to (**d-1**) show the revolution linear velocity of the entire drill string at rotational speeds of 40, 60, 80, and 100 rpm. Negative values denote forward revolution; positive values denote backward revolution. Subplots (**a-2**) to (**d-2**) present the lateral acceleration of the lower 1000 m drill string at the corresponding rotational speeds.

Two additional points require clarification. First, in this simulation set, no significant forward whirling was observed even when the friction coefficient between the drill string and the wellbore was set to zero, which is attributed to excessive clearance. Second, although an increased rotational speed enhances the likelihood of backward whirling, this conclusion holds only under specific conditions. When a higher WOB induces buckling in the drill collar, the drill string demonstrates more complex vibrational modes, as will be discussed in detail in a subsequent section.

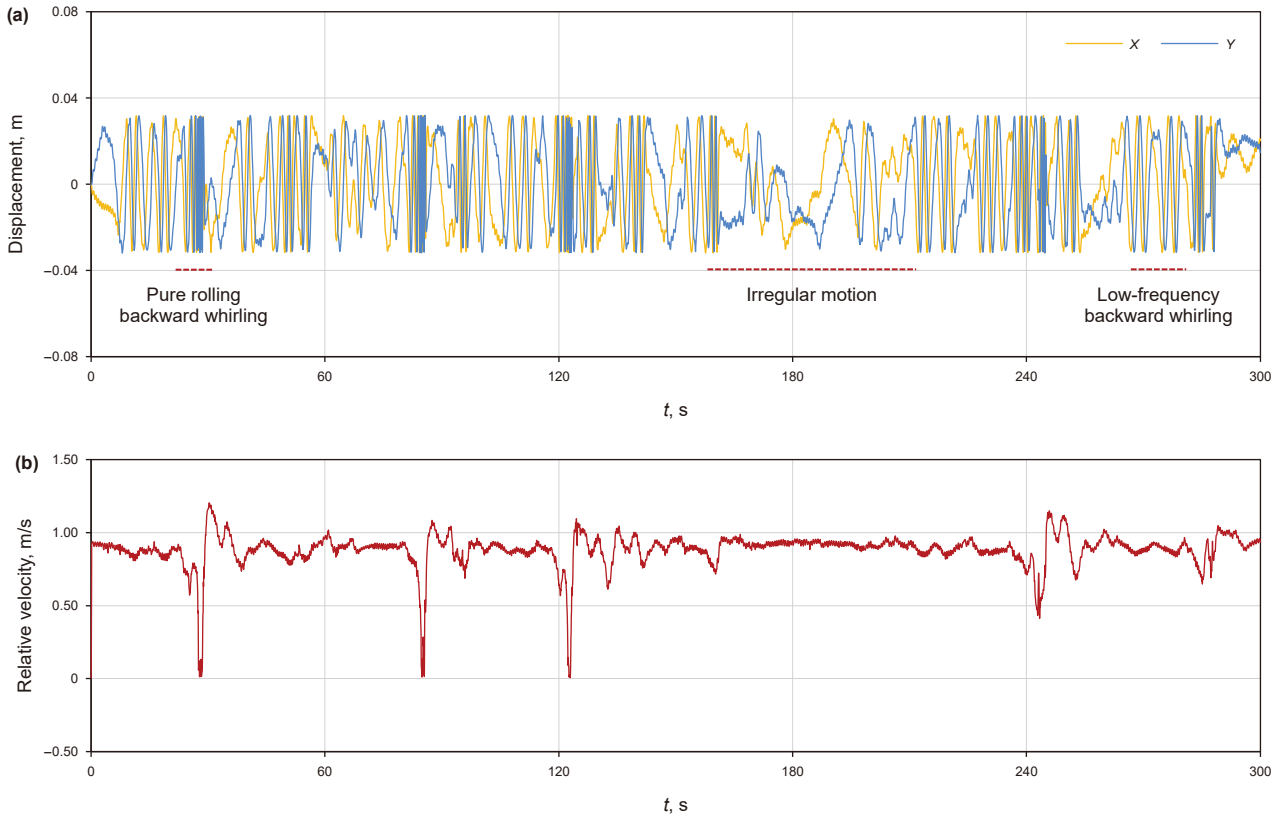

Fig. 8. Lateral displacement and relative velocity of the cross-sectional centroid at a distance of 10 m from the drill bit under the conditions of 100 rpm and 50 kN. (**a**) Lateral displacement. (**b**) Relative velocity.

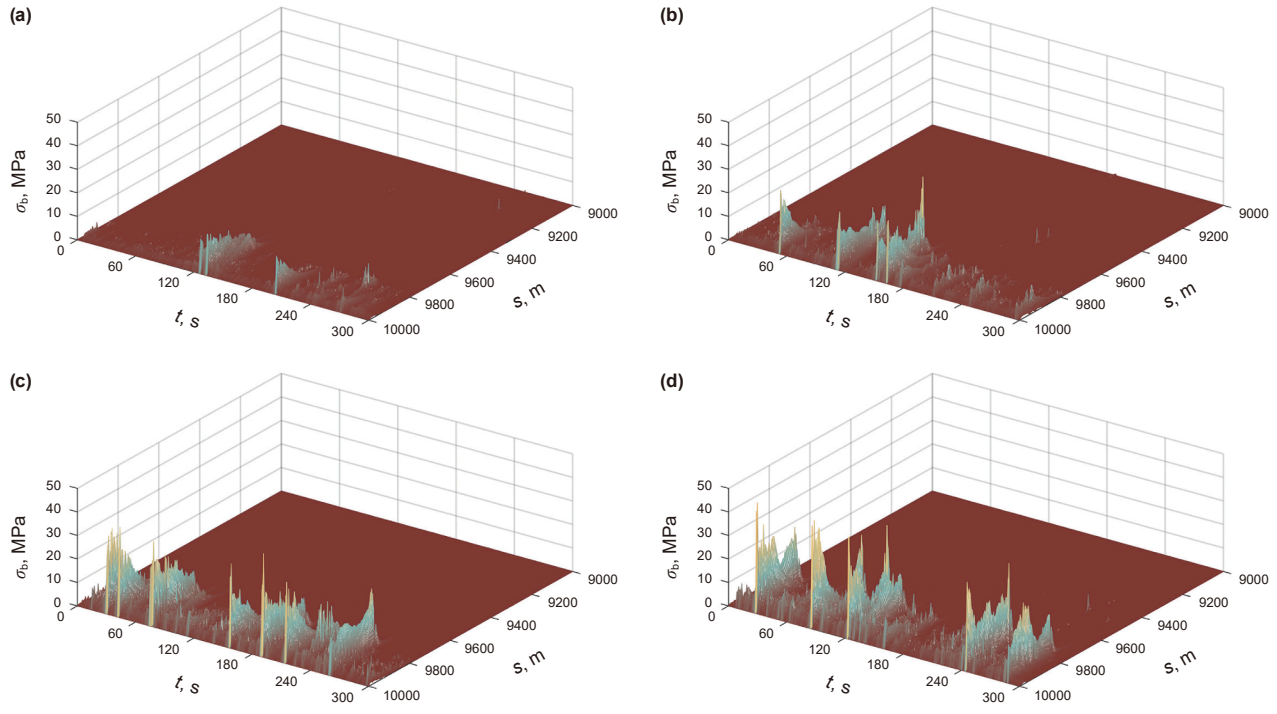

Fig. 9. Variation in the bending stress with increasing rotational speed under a WOB of 50 kN. (**a**) 40 rpm. (**b**) 60 rpm. (**c**) 80 rpm. (**d**) 100 rpm.

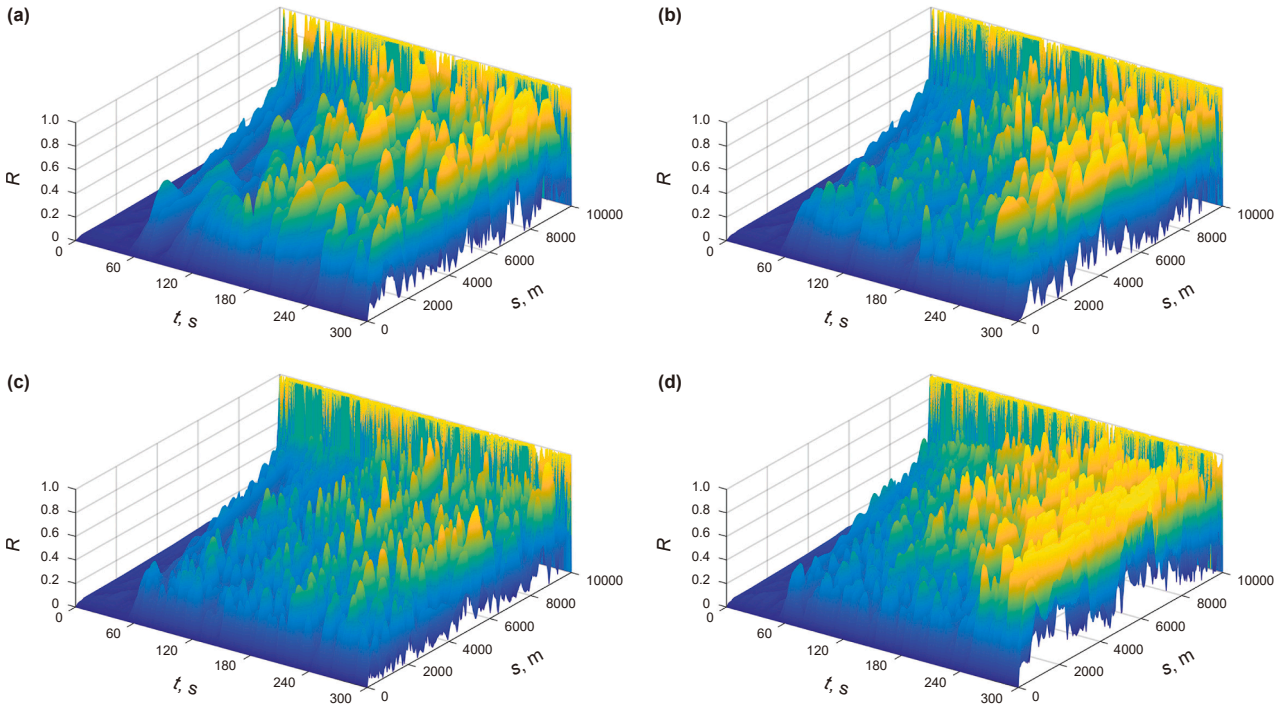

Fig. 10. Variation in the lateral deviation ratio with increasing rotational speed under a WOB of 50 kN. (**a**) 40 rpm. (**b**) 60 rpm. (**c**) 80 rpm. (**d**) 100 rpm.

3.4. Effect of WOB

Based on the BHA configuration provided in Table 2, under a constant rotational speed of 60 rpm, the dynamic characteristics of the entire drill string are presented in Fig. 11 as the WOB increases from 70 to 130 kN. Within the WOB range of 70–90 kN, the number of revolution linear velocity peaks in the drill collar section moderately increases with increasing WOB. However, when the WOB reaches 110 kN, continuous nonnegative peaks emerge in the revolution linear velocity of the drill collar. At this stage, the drill collar experiences high-speed backward whirling with a period of approximately 0.36 s (see Fig. 12). On the basis of the relationship between the backward whirling frequency and rotational frequency, the backward whirling frequency and period at 60 rpm are calculated as 2.8 Hz and 0.357 s, respectively, indicating that the drill collar has entered a stable pure-rolling backward whirling state.

As shown in Fig. 12, compared with the quasi-static helical buckling of the full-length drill pipe simulated in Section 3.2 (see Fig. 6), the drill collar under pure-rolling backward whirling also exhibits helical deformation and sustained bending stress (see Fig. 13(a)). However, its significantly amplified acceleration characteristics indicate that the most intense lateral vibrations occur in this stage (see Fig. 11(c-2)). Furthermore, when the lower drill string experiences high-frequency backward whirling, the resulting transverse waves are unable to propagate upward from the bottom. Consequently, the lateral displacement rate of the upper drill pipe remains substantially lower than that observed during alternating high- and low-frequency lateral vibrations, as demonstrated in Fig. 13(b).

In this simulation set, a notable observation emerges: when the WOB increases to 130 kN, the decay trends of the revolution linear velocity v_t and acceleration a_r indicate that continuous pure-rolling backward whirling does not occur (see Figs. 11(d-1, d-2)). To further investigate this behavior, simulations are conducted at a rotational speed of 100 rpm with WOB values of 50, 70, 110, 130, and 170 kN. The dynamic characteristics of the entire drill string under these conditions are presented in Fig. 14. Analysis of the revolution linear velocity trends in Fig. 14((a-1)–(e-1)) reveals that the critical WOB required for the drill collar section to enter pure-rolling backward whirling decreases with increasing rotational speed. Specifically, as the rotational speed increases from 60 to 100 rpm, the critical WOB decreases from 110 to 70 kN (see Fig. 14(b-1)). Beyond this critical WOB, the pure-rolling backward whirling phenomenon becomes suppressed as the WOB increases further.

On the basis of the simulation data, ESD analysis was performed on the lateral displacement of the drill collar centroid 10 m from the bit under WOB conditions of 50, 70, 110, 130, and 170 kN. By analyzing the time-domain lateral displacement and ESD characteristics during the stable phase of the drill collar, the motion state during WOB escalation can be categorized into three stages:

1) Stage 1 (50–70 kN). At a WOB of 50 kN, the ESD is distributed across 0–2 Hz without a dominant peak. The time-domain signal exhibits a symmetrical amplitude distribution, indicating irregular drill collar motion characterized by low-frequency backward whirling or alternating forward and backward movement (see Fig. 15(a)). When the WOB increases to 70 kN, the energy is concentrated in the 3–5 Hz range, with a peak at 4.36 Hz close to the pure-rolling backward whirling frequency of 4.67 Hz (see Fig. 15(b)). This energy concentration correlates with the most severe lateral vibration observed in the drill collar (see Fig. 14(b)).
2) Stage 2 (110 kN). The dominant peak splits into a low-frequency band (0–1 Hz) and a 1.66 Hz peak, the latter corresponding to the rotational frequency at 100 rpm (see Fig. 15(c)). On the basis of the critical helical buckling load formula, the calculated buckling threshold for the rotating drill collar is 76.6 kN, and the current WOB exceeds this value. Although the simulations of quasi-static helical buckling in

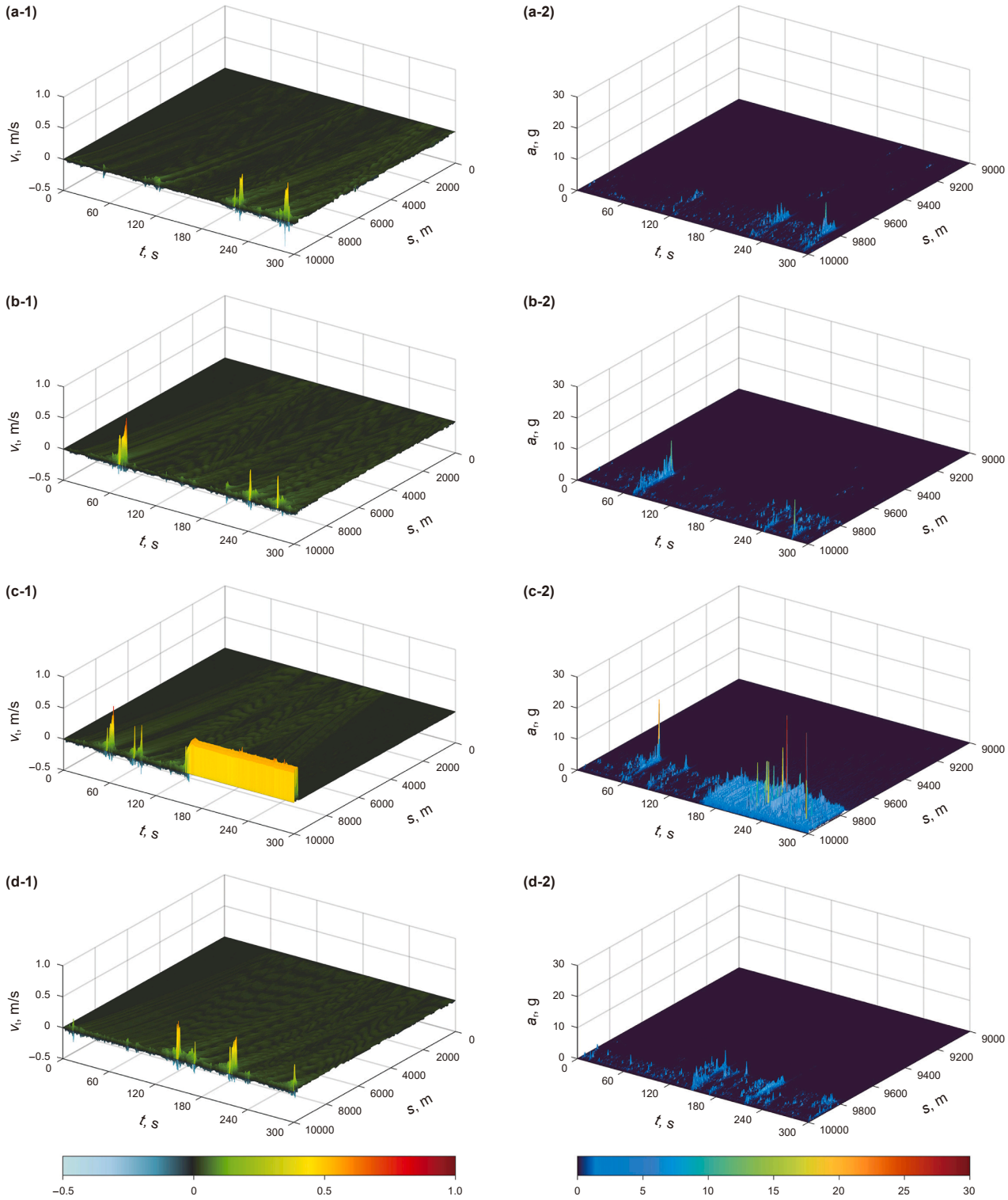

Fig. 11. Evolution of drill string dynamic characteristics with increasing WOB at a rotational speed of 60 rpm. Subplots (**a-1**) to (**d-1**) show the revolution linear velocity of the entire drill string at WOB values of 70, 90, 110, and 130 kN. Negative values denote forward revolution; positive values denote backward revolution. Subplots (**a-2**) to (**d-2**) present the lateral acceleration of the lower 1000 m drill string at the corresponding rotational speeds.

Section 3.2 indicate that buckled drill pipes exhibit extremely low-frequency wall-contact revolution, the amplitude of the lateral displacement time-domain signal in this case remains smaller than the clearance of ±0.0318 m, suggesting the absence of stable helical buckling (see Fig. 16(a)). This indicates that the complex energy distribution results from the transfer of backward whirling energy to low-order buckling modes as the WOB surpasses the critical buckling load. Simultaneously, centrifugal forces from rotation, as evidenced by the 1.66 Hz ESD peak, counteract this energy transfer by sustaining backward whirling. Therefore, this stage is identified as the “modal competition” phase.

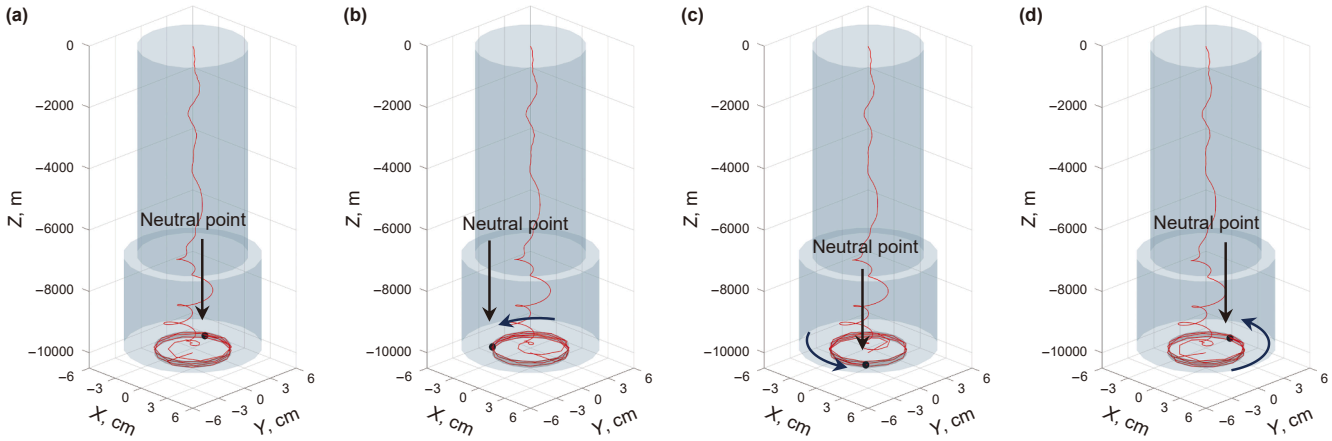

Fig. 12. Motion state of the drill string during one revolution cycle of 0.36 s at 60 rpm and 110 kN. (**a**–**d**) Lateral vibrations of the drill string at 242.35, 242.45, 242.55, and 242.70 s, respectively. The transparent blue cylinder represents the clearance between the drill string and the wellbore wall. The red solid line indicates the centerline of the drill pipe. The blue arrow shows the direction of motion of the drill string. The black solid circle marks the current position of the neutral point.

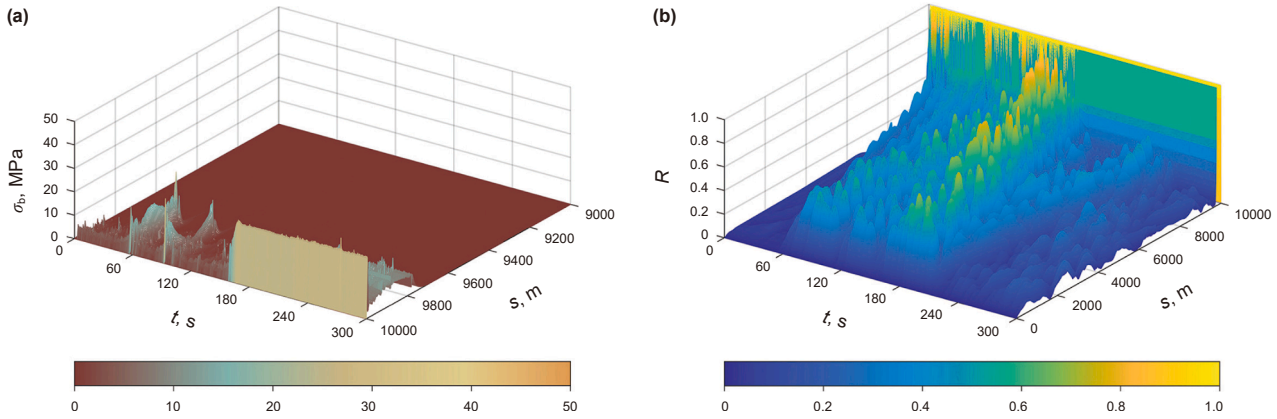

Fig. 13. Dynamic characteristics of the drill string at 60 rpm and 110 kN. (**a**) Bending stress. (**b**) Lateral deviation ratio.

3) Stage 3 (130–170 kN). The ESD dominant peak gradually shifts toward lower frequencies, accompanied by energy amplitudes exceeding 1.66 Hz. The lateral displacement amplitude approaches the clearance, indicating that buckling modes become dominant in the modal competition (see Fig. 15(d) and (e)). However, this helical buckling state differs from the full-length drill pipe buckling simulated earlier; the drill collar displays low-frequency forward revolution (see Fig. 16(b)).

On the basis of the simulations presented in this section, the following patterns can be summarized: when the WOB is below the critical load for helical buckling, the development of backward whirling intensifies with increasing WOB, as evidenced by significant increases in vibration acceleration and bending stress. When the WOB exceeds the critical load for helical buckling, the compressed drill string enters a modal competition stage between helical buckling and backward whirling, during which the revolution linear velocity and vibration acceleration decrease markedly, and the characteristics of helical buckling become increasingly dominant as the WOB continues to increase.

To validate the reliability of these findings, field data from an ultra-deep well in the Tarim Oilfield were analyzed. The test interval spanned from 8442.56 to 8447.01 m, with a wellbore diameter of 0.241 m. The drill collar and upper drill pipe dimensions corresponded to those listed in Table 2. A downhole memory-type vibration measurement sub was installed 3 m above the drill bit to record the root mean square values of the lateral vibration acceleration (GRMS) at a sampling frequency of 1000 Hz. In terms of signal processing, the per-minute data were divided into several equal-width time windows. Abnormal signals exceeding the maximum measurement range were processed using a moving average method, and the GRMS value within each time window was calculated. Finally, the maximum value among them was selected as the vibration severity indicator for that time period. The logging data were sampled at 1 Hz. Based on the variations in the rotational speed and WOB during the sampling period, the 120-min interval was divided into four stages (see Fig. 17(a)). The corresponding lateral vibration GRMS for each stage are presented in Fig. 17(b).

1) Stage I (0–9 min). Off-bottom rotation at 30 rpm. GRMS remained stable at approximately 3 g.
2) Stage II (9–28 min). Off-bottom rotation at 45 rpm. GRMS increased significantly compared with Stage I, indicating that a higher rotational speed exacerbated lateral vibrations.
3) Stage III (28–45 min). Initial contact with the well bottom. The rotational speed was fine-tuned to 49 rpm, and the initial increase in WOB compressed the lateral vibration space as the drill bit engaged the formation, resulting in a slight decrease in acceleration. As the WOB continued to increase, GRMS reached

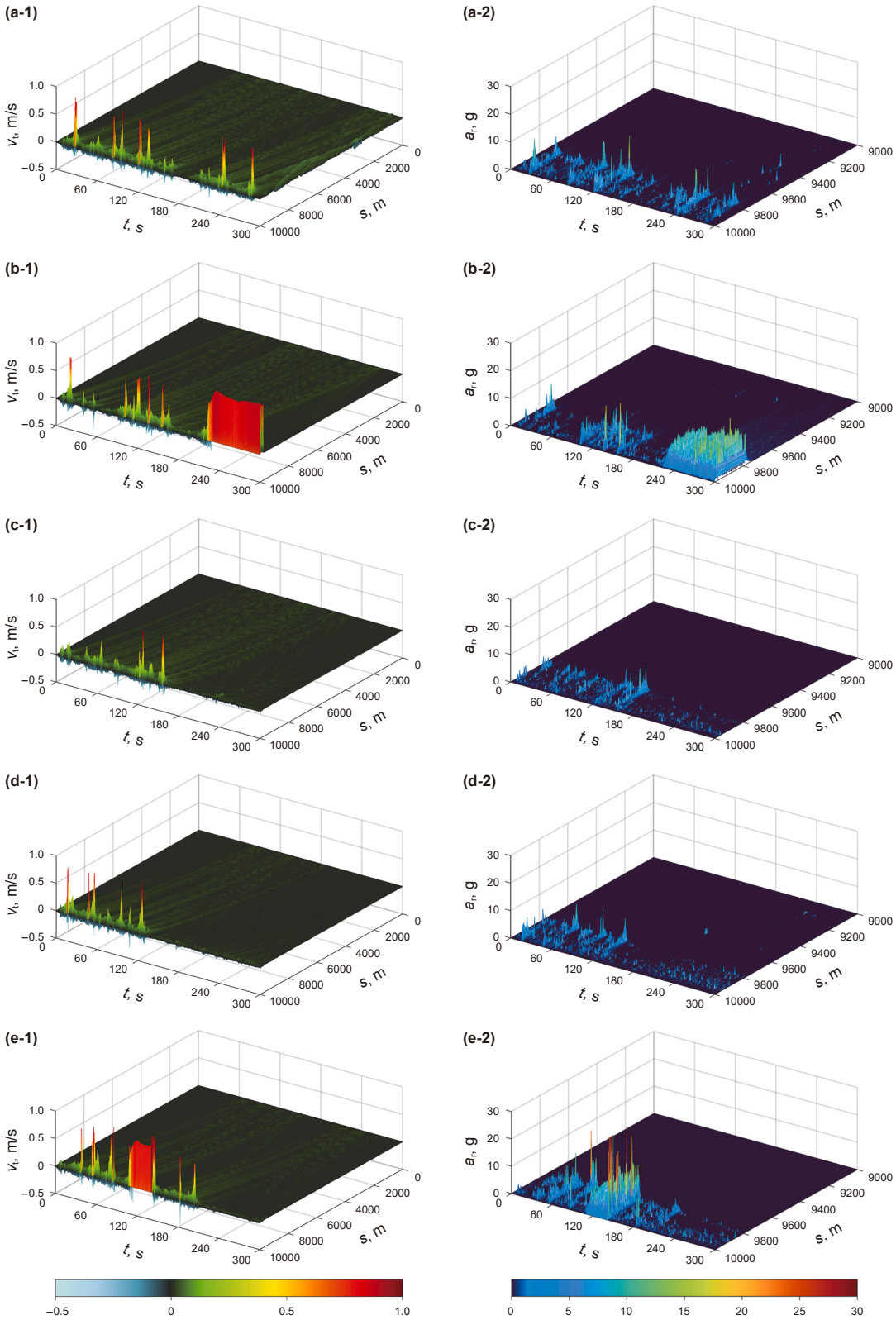

Fig. 14. Evolution of drill string dynamic characteristics with increasing WOB at a rotational speed of 100 rpm. Subplots (**a-1**) to (**e-1**) show the revolution linear velocity of the entire drill string at WOB values of 50, 70, 110, 130, and 170 kN. Negative values denote forward revolution; positive values denote backward revolution. Subplots (**a-2**) to (**e-2**) present the lateral acceleration of the lower 1000 m drill string at the corresponding rotational speeds.

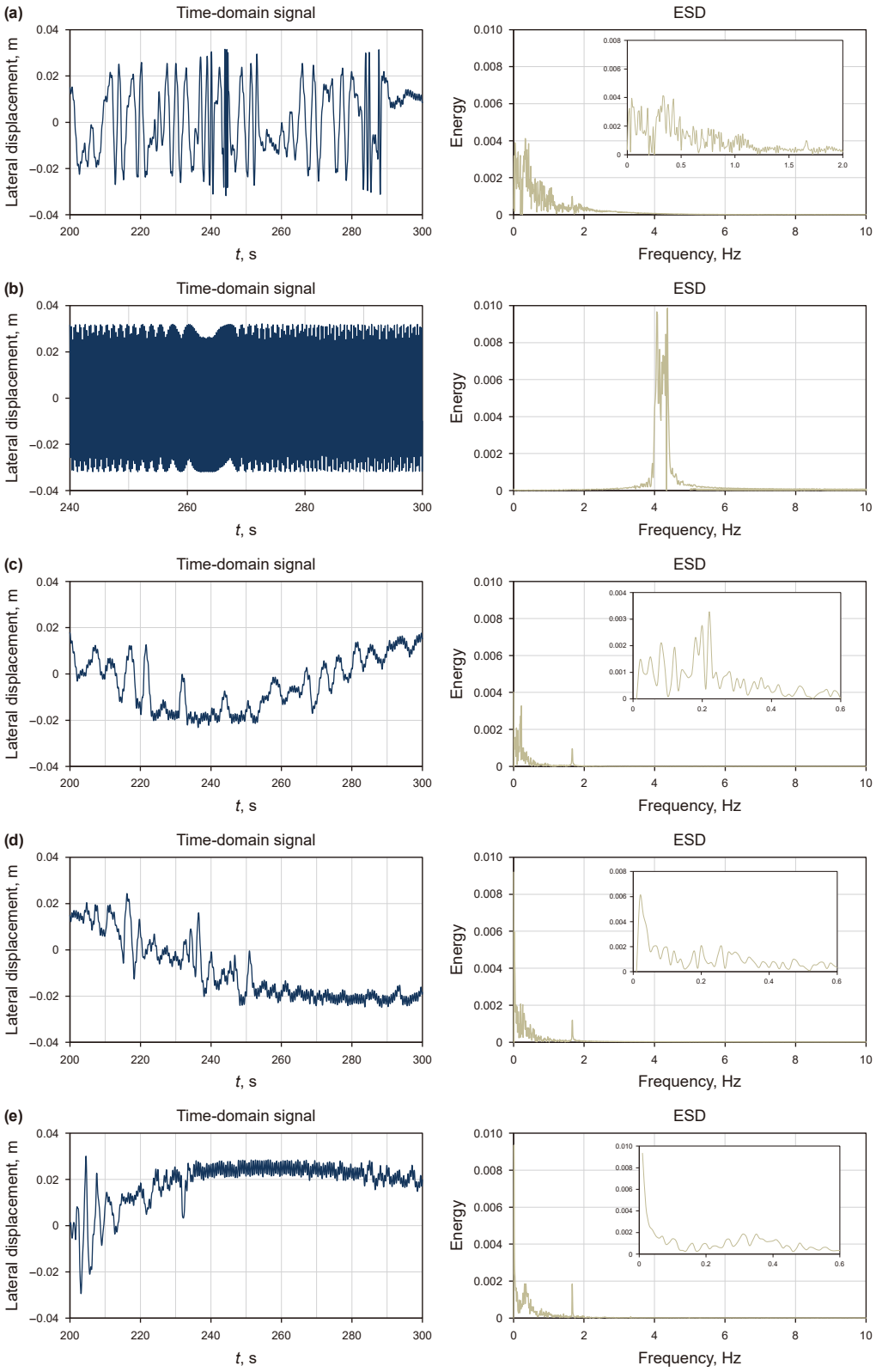

Fig. 15. Lateral displacement time-domain signals and corresponding ESDs under different WOB. (**a**) 50 kN. (**b**) 70 kN. (**c**) 110 kN. (**d**) 130 kN. (**e**) 170 kN.

a peak of 10 g before an inflection point occurred, eventually decreasing to 5 g at 120 kN.

4) Stage IV (45–120 min). Rotary drilling at 49 rpm with WOB ranging from 110 to 150 kN. GRMS further decreased initially and remained consistently lower than that in the previous stages. Sampling was automatically suspended during two intervals (73–86 min and 88–102 min) because the vibration signals fell below 0.9 g, indicating relatively stable vibration

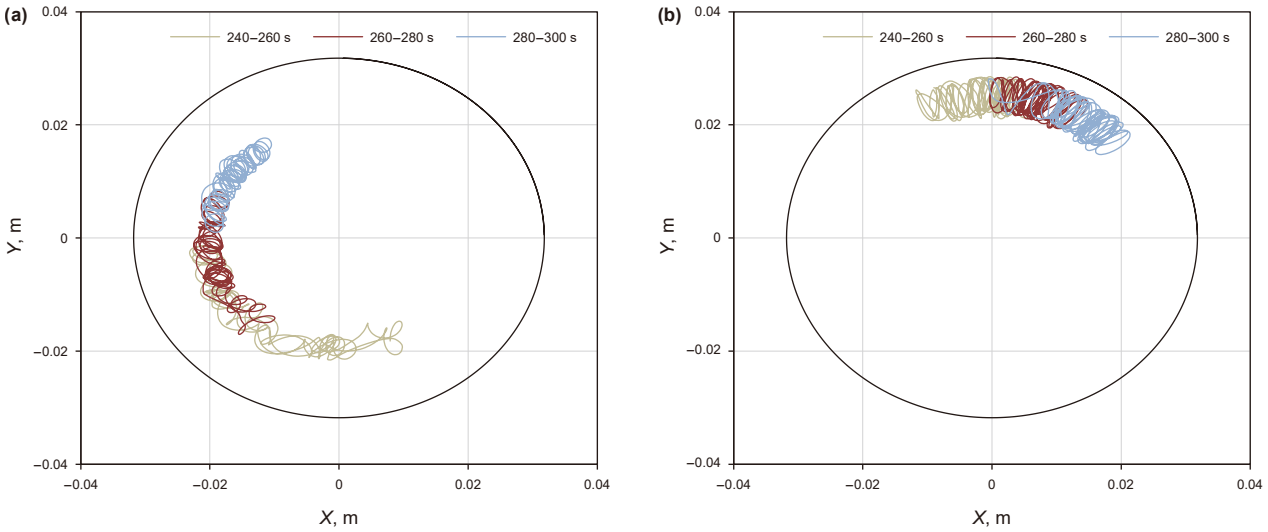

Fig. 16. Lateral displacement of the cross-sectional centroid under different WOB. (**a**) 110 kN. (**b**) 170 kN. The black circle represents the clearance between the drill collar and wellbore. The three colored curves inside the circle depict the motion trajectories of the drill collar centroid 10 m from the drill bit during different time periods.

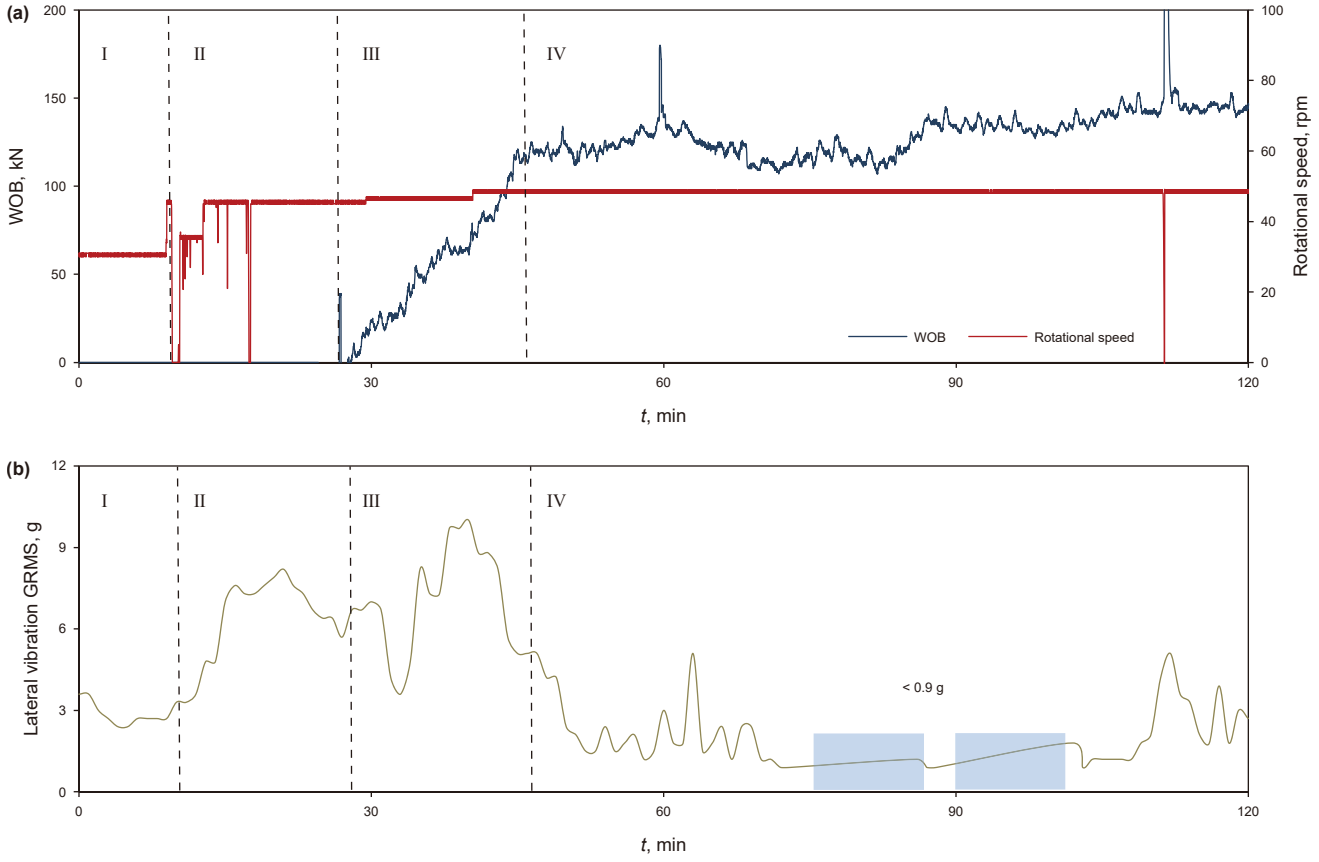

Fig. 17. Downhole-measured lateral vibration GRMS during rotational speed and WOB adjustments. (**a**) Time-domain signals of rotational speed and WOB, sampling frequency is 1 Hz. (**b**) Time-domain signal of lateral vibration GRMS, sampling frequency is 1000 Hz. Blue areas: signals below the lower measurement range limit. Downhole signal processing: per-minute data divided into equal windows, with outliers processed by a moving average and the maximum GRMS value selected.

levels throughout this phase. The trend of increased WOB leading to vibration intensity that first intensifies and then attenuates is consistent with the conclusions of this study. The underlying mechanism can be explained by modal competition, which further validates the accuracy of the model calculations.

On the basis of these patterns, a parameter optimization strategy suitable for ultra-deep well drilling safety and efficiency can be proposed. From the vibration suppression perspective, maintaining the drill string in a modal competition state helps avoid high-speed backward whirling and results in substantially

lower lateral acceleration than in pure whirling conditions. This effectively reduces drill string damage caused by impact and wear—particularly the full-circumferential wear typical of rolling motion—while helping preserve wellbore integrity. To improve the drilling efficiency, modal competition can be induced by applying a WOB that exceeds the critical helical buckling load. Increasing the rotational speed further promotes the onset of modal competition at relatively lower WOB values, thereby enhancing the ROP. In terms of drill string safety, the bending stress during modal competition remains lower than that under backward whirling (see Fig. 18), which more effectively prevents fatigue and fracture caused by excessive bending. Therefore, rationally adjusting the WOB and rotational speed to induce and maintain modal competition offers a practical and effective method for optimizing drilling parameters in ultra-deep well operations.

3.5. Effect of the stabilizer

In BHA design, the optimal axial positioning of near-bit stabilizers is critical for maintaining drill string stability and controlling the wellbore trajectory. This aspect is especially vital in deep drilling operations, where it directly affects operational safety and wellbore quality. Mechanically, the deviation correction mechanism of stabilizers follows the pendulum effect, with the recommended installation range generally being confined to 1–3 lengths of a single drill collar. Within this mechanical framework, a comparative analysis was performed using the BHA configuration specified in Table 2, where full-gauge stabilizers with a length of 1 m and an outer diameter of 0.239 m are positioned at distances of 10, 15, 20, 25, and 30 m from the bit. The rotational speed and WOB were set to 100 rpm and 70 kN, respectively, representing the severe vibration and high-stress backward whirling conditions illustrated in Figs. 14(b) and 18(a) in Section 3.4.

Based on the dynamic characteristics analysis in Fig. 19, when the revolution linear velocity v_t and lateral acceleration a_r are used as evaluation metrics for vibration intensity, the drill string exhibits the most severe lateral vibration when the stabilizer is installed 10 m above the bit. As the stabilizer position moves upward, the lateral vibration of the drill string system exhibits a nonlinear trend, initially decreasing and then increasing. The optimal vibration suppression effect is achieved when the stabilizer is positioned 20 m from the bit. Notably, when the stabilizer is placed 30 m above the bit, backward whirling begins to occur in the upper drill pipe. This finding indicates that further upward relocation of the stabilizer gradually reduces both the deviation correction capability and vibration damping effectiveness of the BHA.

Fig. 20(a) shows the time-domain signal of the lateral displacement of the stabilizer centroid when it is positioned 15 m from the bit. On the basis of the characteristics of this signal, the motion states of the full-gauge stabilizer can be divided into two categories, with Fig. 20(b) and (c) illustrating the corresponding centroid trajectories within the wellbore. Owing to the narrow clearance between the stabilizer and the wellbore, the motion of the stabilizer is dominated by forward whirling (see Fig. 20(b)), which corresponds to the time intervals in Figs. 19(b-1, b-2) characterized by a lower revolution linear velocity and lateral acceleration. As analyzed in Section 3.3, when the drill string experiences backward whirling, both revolution linear velocity and lateral acceleration increase significantly. The time intervals in Figs. 19(b-1, b-2) exhibiting such elevated vibration levels correlate with the occurrence of the stabilizer backward whirling (see Fig. 20(c)), indicating that the stabilizer is driven into this motion by vibrations transmitted from the adjacent drill collar. In this study, the contact between the drill string and the wellbore is assumed to be inelastic. Despite assigning a high wellbore stiffness coefficient of 10^8 N·m^{-1} in the simulation, the centroid trajectory of the stabilizer still exceeds the clearance. This implies that the full-gauge stabilizer generates an extremely high contact force against the wellbore during backward whirling, which may lead to wellbore enlargement or even collapse.

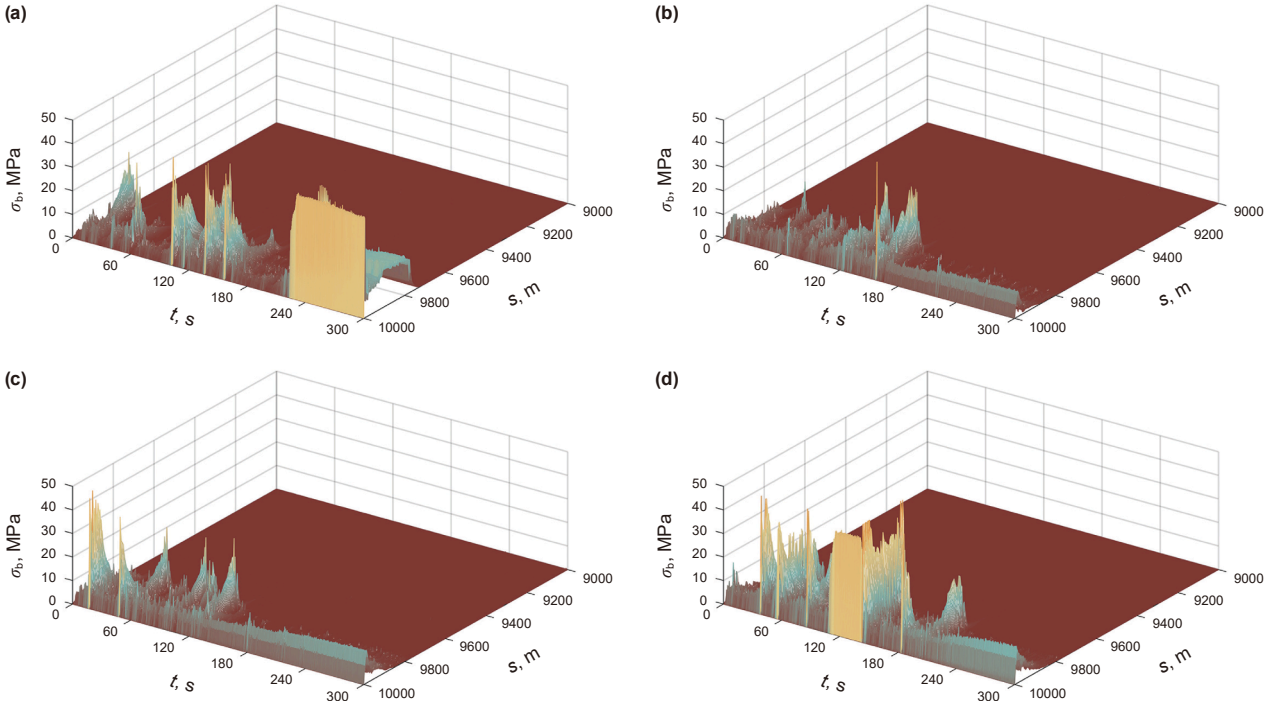

Fig. 18. Variation in the bending stress with increasing WOB at a rotational speed of 100 rpm. (**a**) 70 kN. (**b**) 110 kN, modal competition state. (**c**) 130 kN. (**d**) 170 kN.

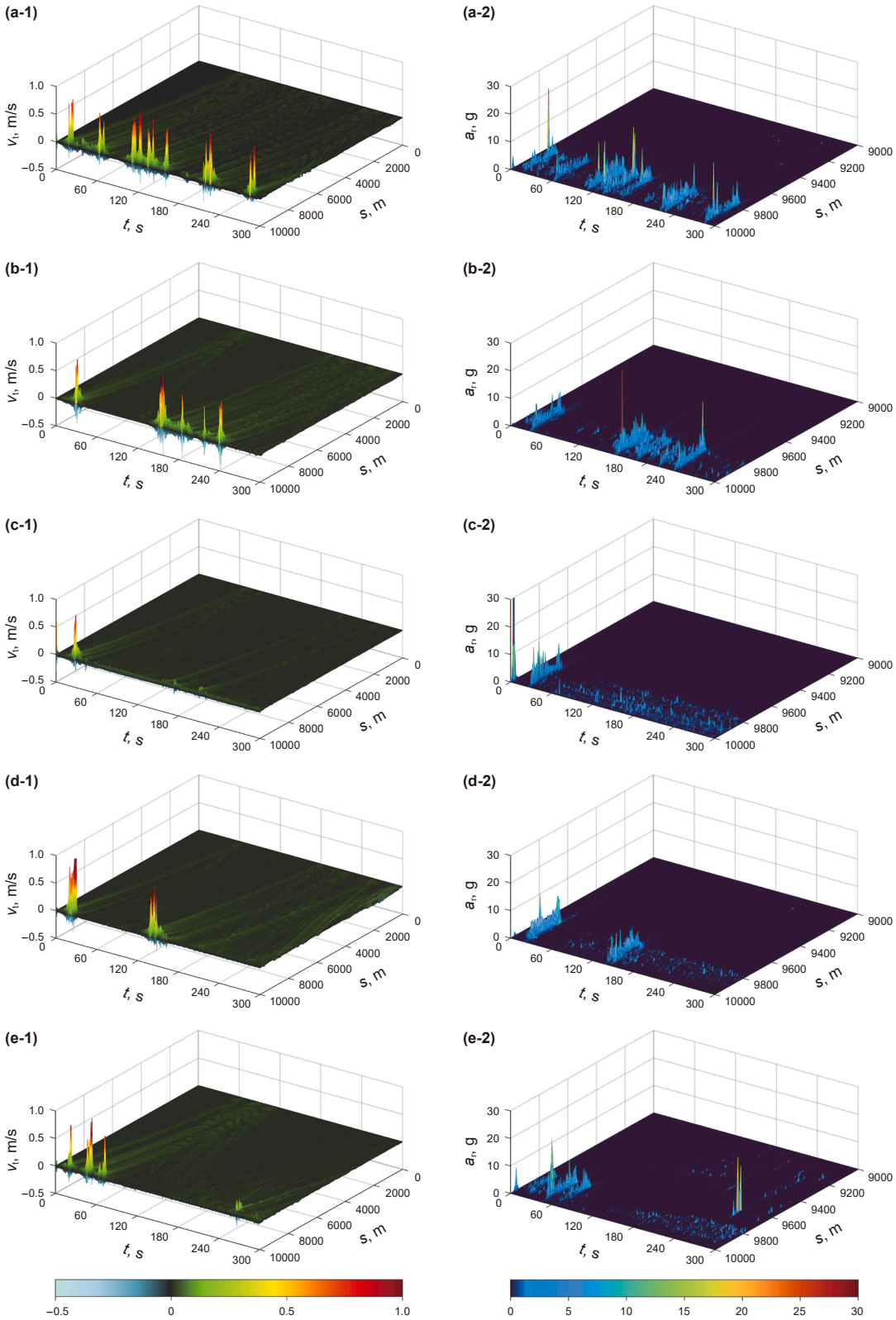

Fig. 19. Evolution of drill string dynamic characteristics with increasing stabilizer-to-bit distance at 100 rpm and 70 kN (stabilizer outer diameter: 0.239 m). Subplots (**a-1**) to (**e-1**) show the revolution linear velocity of the entire drill string at stabilizer positions of 10, 15, 20, 25, and 30 m. Subplots (**a-2**) to (**e-2**) present the lateral acceleration of the lower 1000 m drill string at corresponding rotational speeds and WOB.

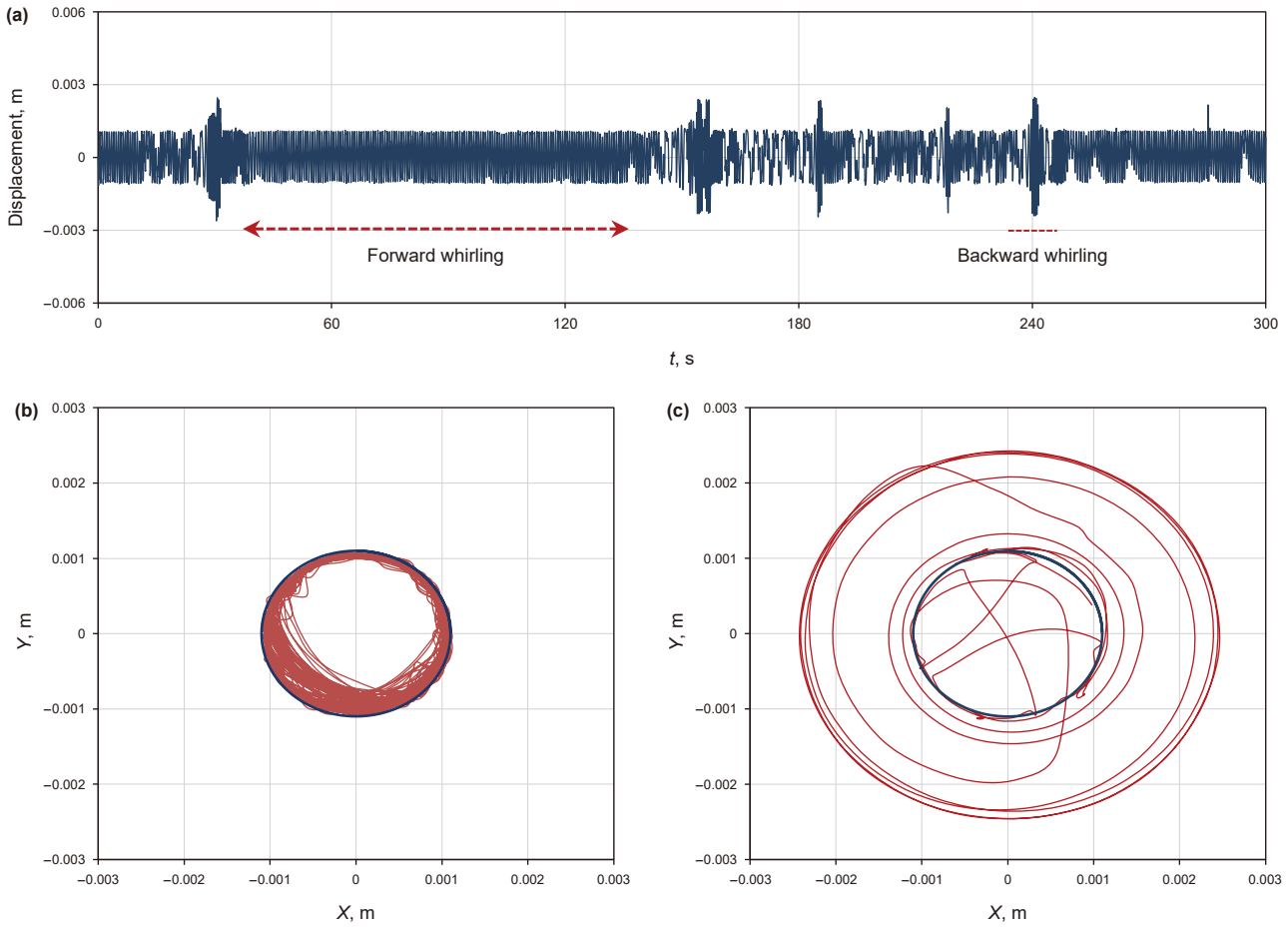

Fig. 20. Motion state of a stabilizer under the conditions of 100 rpm and 70 kN (stabilizer diameter: 0.239 m. Stabilizer-to-bit distance: 15 m. Black circles: stabilizer-wellbore clearance. Red curves: motion trajectory of the centroid). (**a**) Time-domain signal of the centroid lateral displacement of the stabilizer. (**b**) Forward whirling from 60 to 120 s. (**c**) Backward whirling from 239 to 241 s.

In addition to optimizing the position of the full-gauge stabilizer, this study further investigates vibration control strategies for pendulum BHAs. Using a BHA with a stabilizer positioned 15 m above the bit, the effects of varying the stabilizer outer diameter under conditions of a 100 rpm and 70 kN are examined. The diameters considered include near-full-gauge (0.235 m) and under-gauge configurations (0.231, 0.220, and 0.200 m). The resulting trends in the BHA's dynamic behavior are illustrated in Fig. 21. For comparative purposes, the simulations for full-gauge stabilizers and stabilizer-free BHAs under identical operating conditions are presented in Figs. 19(b-1, b-2) and 14(b-1, b-2), respectively.

Under the current parameter configuration, the vibration intensity of the BHA system tends toward initial reduction followed by aggravation as the stabilizer outer diameter decreases. A significant vibration suppression effect is observed when the stabilizer outer diameter is 0.231 m. However, when the diameter is reduced to 0.200 m, the system transitions into a pure rolling backward whirling state (see Figs. 21(d-1, d-2)), and further reductions lead to vibration characteristics resembling those of stabilizer-free BHAs. These findings indicate that under-gauge stabilizers can serve as a practical alternative to full-gauge stabilizers for vibration mitigation, particularly when the latter are not optimally positioned.

The underlying mechanism of these patterns can be explained by analyzing the motion states of near-full-gauge and under-gauge stabilizers and their adjacent drill collars. Fig. 22 shows the time-domain lateral displacement signals and ESD distributions of the stabilizers and their upper drill collars (located 15 m above) for stabilizer outer diameters of 0.235 and 0.231 m. When the stabilizer outer diameter is 0.235 m, its motion trajectory exhibits well-defined revolution characteristics, with displacement amplitudes consistently constrained within the annular clearance range (±0.003 m). The ESD curve displays a single dominant peak at 1.66 Hz, corresponding to the drill string's rotational frequency at 100 rpm, indicating that the stabilizer operates in a stable forward whirling mode dominated by pure sliding motion (see Figs. 22(a-1)). For the under-gauge stabilizer with an outer diameter of 0.231 m, the ESD distribution significantly changes: in addition to the rotational frequency peak, a distinct low-frequency broadband feature emerges in the 0–1.66 Hz range (see Figs. 22(b-1)). Combined with the aperiodic nature of the time-domain signals, this confirms that the stabilizer enters an irregular motion state involving frequent collisions with the wellbore. Notably, this low-frequency broadband signature also appears in the ESD curves of the upper drill collar (see Fig. 22(b-2)), indicating that the under-gauge stabilizer transmits low-frequency vibrational energy to adjacent collars through lateral wave propagation. This energy transfer disrupts the collar's vibration modes and effectively suppresses backward whirling. In contrast, BHAs equipped with near-full-gauge stabilizers show no significant lateral vibration interference (see Fig. 22(a-2)), resulting in limited overall vibration suppression despite the stabilizer's stable forward whirling. When

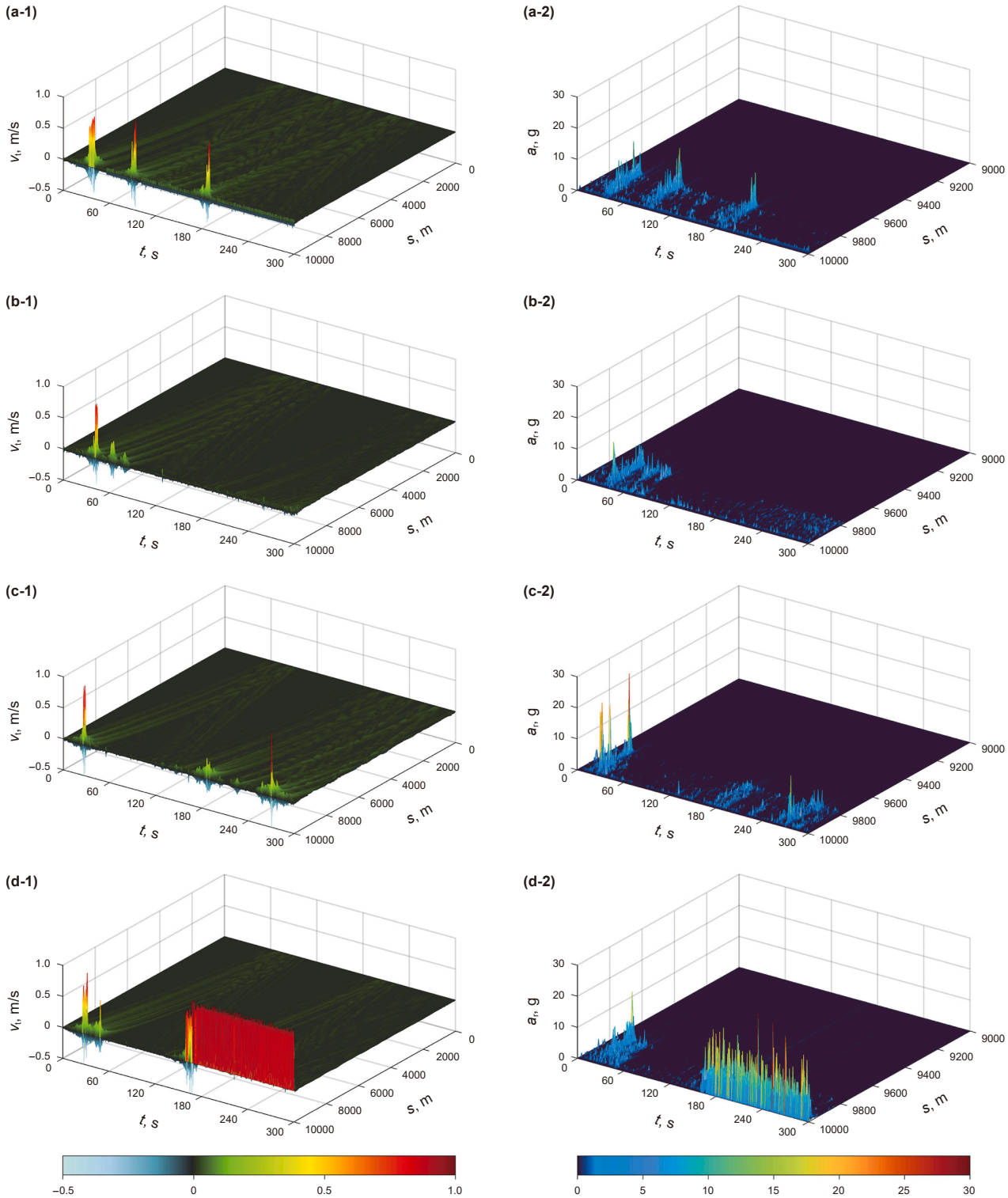

Fig. 21. Evolution of drill string dynamic characteristics with decreasing stabilizer outer diameter at 100 rpm and 70 kN (stabilizer-to-bit distance: 15 m). Subplots (**a-1**) to (**d-1**) show the revolution linear velocity of the entire drill string at stabilizer outer diameters of 0.235, 0.231, 0.220, and 0.200 m. Subplots (**a-2**) to (**d-2**) present the lateral acceleration of the lower 1000 m drill string at the corresponding rotational speeds and WOB.

the stabilizer outer diameter is further reduced to 0.200 m, both the stabilizer and upper collar transition into backward whirling. This finding coherently explains the nonlinear trend observed in Fig. 21, where the lateral vibration intensity initially decreases but eventually intensifies with decreasing stabilizer size.

The motion state of the stabilizer tends to transition from forward whirling through irregular motion to backward whirling as the outer diameter gradually decreases. This pattern is consistent with the current understanding of how lateral vibration is affected by wellbore clearance. Fig. 23 illustrates the bending stress

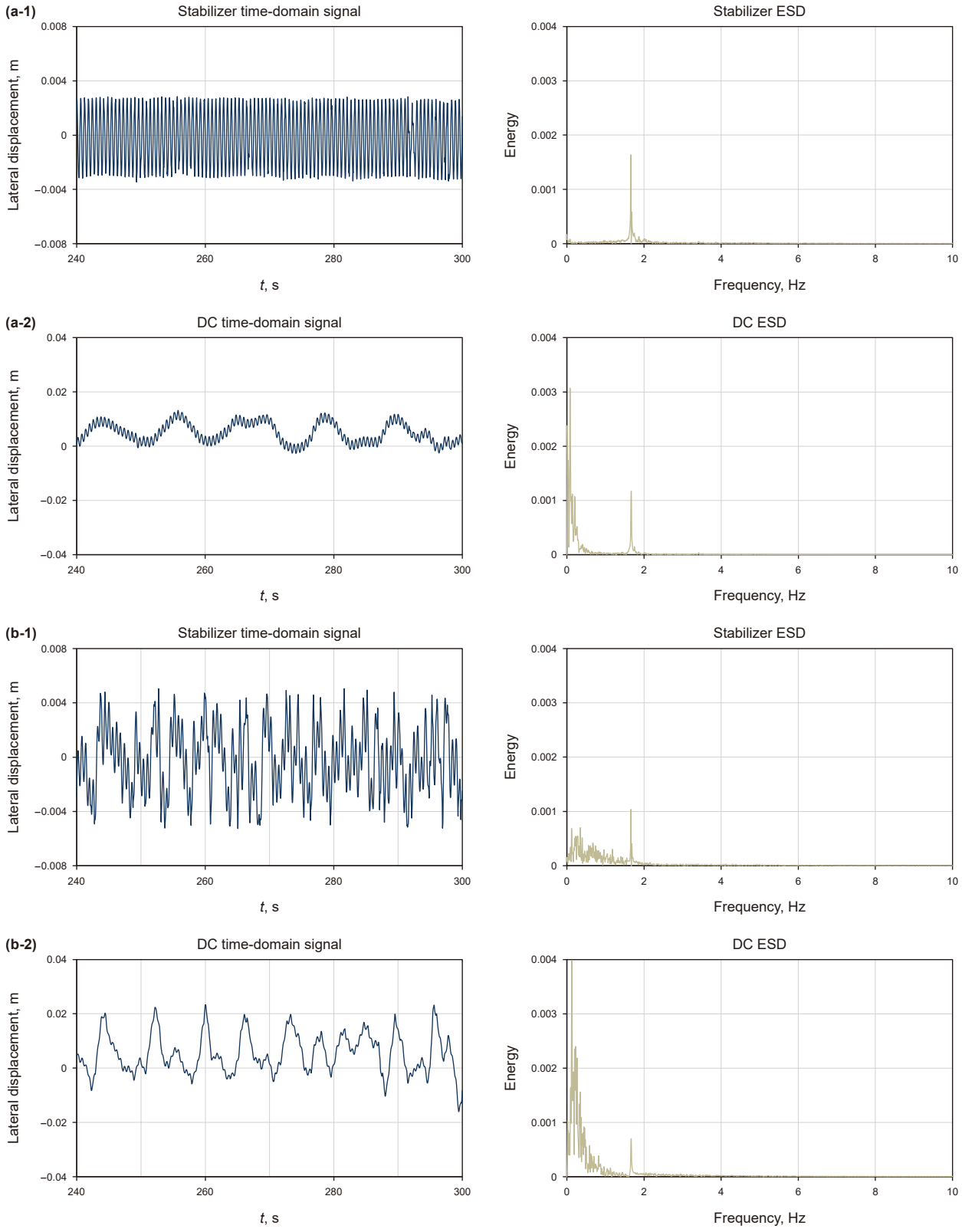

Fig. 22. Lateral displacement time-domain signals and corresponding ESD of the stabilizer and upper drill collar for different stabilizer sizes. (**a-1**) 0.235 m outer diameter stabilizer. (**a-2**) Drill collar above the 0.235 m stabilizer. (**b-1**) 0.231 m outer diameter stabilizer. (**b-2**) Drill collar above the 0.231 m stabilizer.

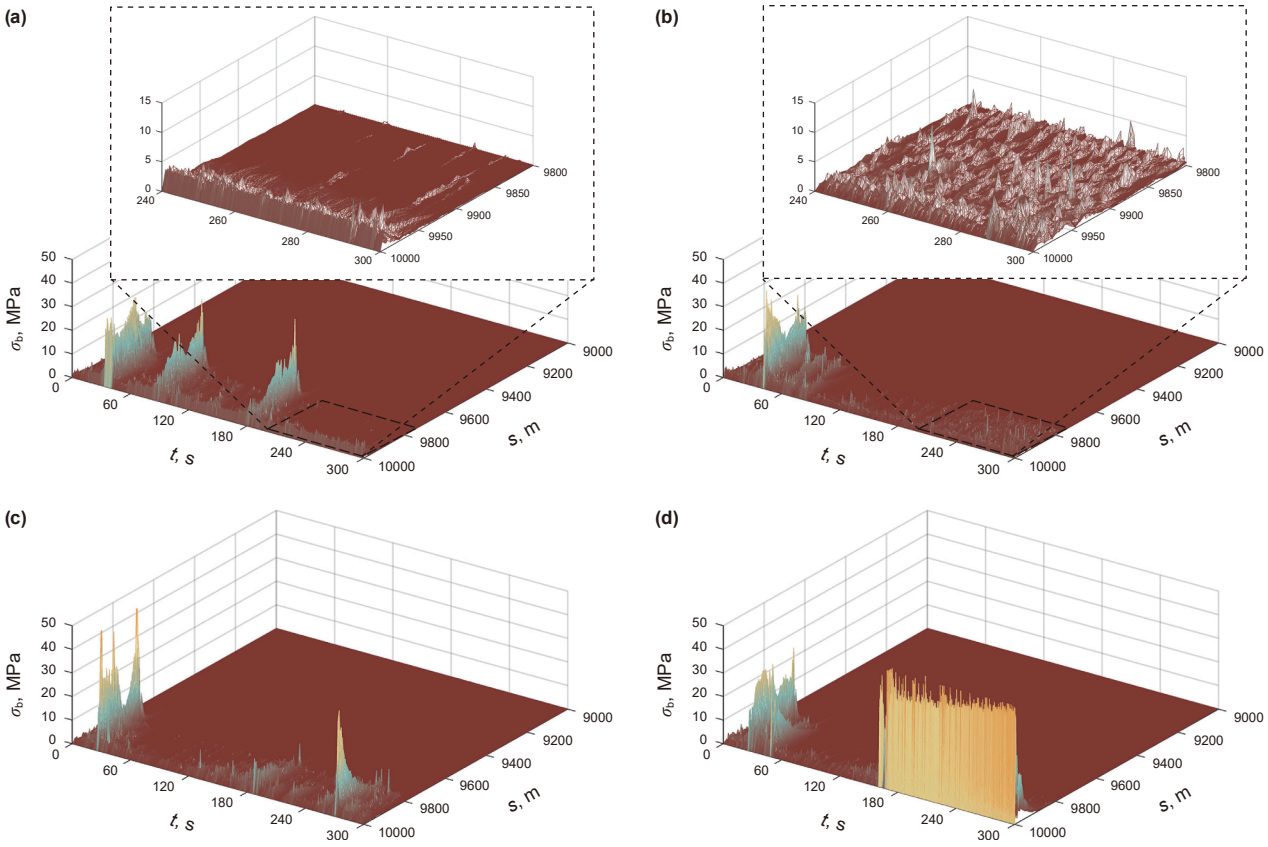

Fig. 23. Variation in the bending stress with decreasing stabilizer outer diameter. (**a**) 0.235 m, forward whirling. (**b**) 0.231 m, irregular motion. (**c**) 0.220 m, near-backward whirling. (**d**) 0.200 m backward whirling.

distribution characteristics of the BHA system under different whirling states. The simulation results show that when the stabilizer is in forward whirling or irregular motion states, its maximum bending stress is significantly lower than that during backward whirling or near-backward whirling states, with marked differences in the stress distribution patterns. Specifically, in the forward whirling state, although continuous stress peaks are present, their amplitudes remain relatively low (see Fig. 23(a)). Irregular motion is characterized by minor, discontinuous stress fluctuations. This stress dispersion effect helps distribute loads across various sections of the BHA, forming an effective stress buffer (see Fig. 23(b)). In contrast, backward whirling produces concentrated high-amplitude stresses, which pose a serious threat to the structural integrity of the drill string (see Fig. 23(d)).

On the basis of the simulation results in Fig. 21, the under-gauge stabilizer with an outer diameter of 0.231 m is identified as the optimal choice in this set of simulations. This method—adjusting the stabilizer size to maintain a non-whirling state and create vibration interference with adjacent drill pipes—has potential for vibration suppression. With the stabilizer outer diameter fixed at 0.231 m, its position is varied between 10 and 30 m from the bit to analyze the sensitivity of this under-gauge stabilizer to the installation location. The simulation results are presented in Figs. 24 and 21(b-1, b-2). Compared with the full-gauge stabilizer (see Fig. 19), the vibration intensity of the BHA equipped with the under-gauge stabilizer initially decreases and then increases as the stabilizer moves upward, with the optimal installation distance identified at 15 m from the bit. The key distinction lies in the fact that the under-gauge stabilizer consistently offers superior vibration suppression compared with the full-gauge stabilizer, suggesting a lower sensitivity to the installation location. This characteristic makes the under-gauge stabilizer a more adaptable and flexible option for BHA configuration and optimization.

The preceding analysis of the stabilizer dimensions and positioning effects on vibration was conducted under the most severe conditions. To validate the broader applicability of these findings, comprehensive performance comparisons between full-gauge and under-gauge stabilizers must be performed across diverse drilling parameter combinations. Lateral acceleration time-domain signals were acquired at various locations along the drill string. Following system stabilization, data segments beginning 60 s post-stabilization are partitioned into 10 s intervals. The GRMS was computed for each interval, and the maximum GRMS value was used as the vibration metric. Comparisons of under-gauge versus full-gauge stabilizer performances under different parameter combinations are presented in Table 3, while the GRMS values for the stabilizer-free BHA serve as a benchmark in Table 4.

Table 3 reveals that, with the exception of the under-gauge stabilizer in parameter Combinations 1 and 6, all the other configurations exhibit a consistent trend: the BHA vibration intensity initially decreases and then increases as the stabilizers are relocated upward. The optimal position for full-gauge stabilizers is 20 m above the bit, whereas under-gauge stabilizers perform best at 15 or 20 m (particularly under higher WOB). Except for Combination 1 and instances where full-gauge stabilizers are located at their 20 m optimal position, under-gauge stabilizers consistently demonstrate lower GRMS values than full-gauge types. This implies that under-gauge stabilizers exhibit lower sensitivity to positional deviations while delivering superior overall vibration damping. Cross-referencing Tables 3 and 4 identifies Combination

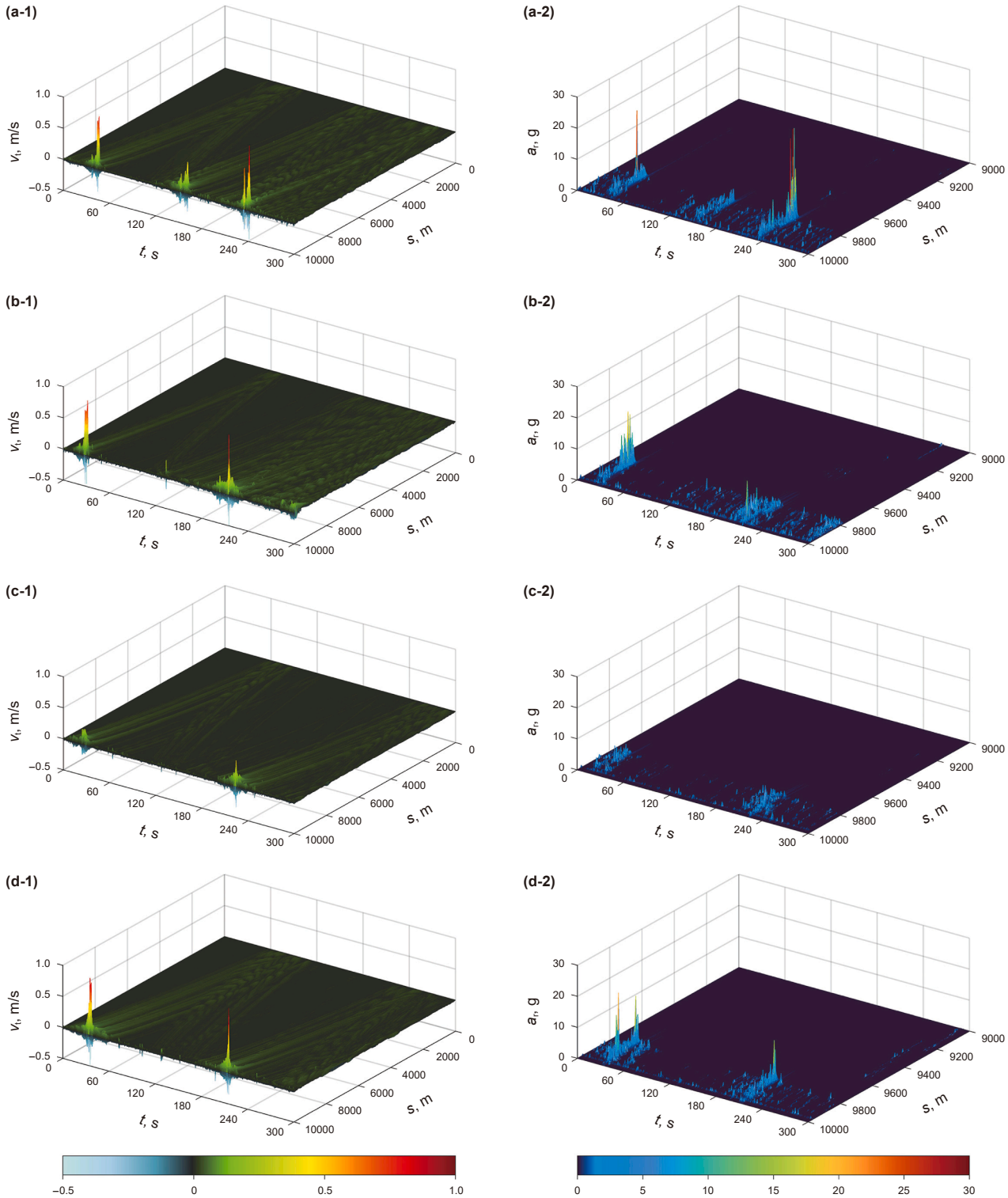

Fig. 24. Evolution of drill string dynamic characteristics with increasing stabilizer-to-bit distance at 100 rpm and 70 kN (stabilizer outer diameter: 0.231 m). Subplots (**a-1**) to (**d-1**) show the revolution linear velocity of the entire drill string at stabilizer positions of 10, 20, 25, and 30 m. Subplots (**a-2**) to (**d-2**) present the lateral acceleration of the lower 1000 m drill string at the corresponding rotational speeds and WOB.

6 as an anomalous case where stabilizers unexpectedly amplify vibrations.

The contradictory observations in parameter Combinations 1 and 6 compared with the previous conclusions stem from the absence of significant lateral vibrations in both cases, as evidenced by the GRMS values of the stabilizer-free BHA. Combination 1 employs a lower rotational speed and WOB, which fails to induce severe whirling (see Fig. 7(a)). In contrast, Combination 6 drives the BHA into a buckling-dominated modal competition phase. Consequently, when the BHA operates in a relatively stable state,

Table 3
Influence patterns of the stabilizer configuration on the lateral vibrations under various drilling parameters.

Number	Rotational speed, rpm	WOB, kN	Stabilizer position, m	Under-gauge GRMS, g	Full-gauge GRMS, g
1	40	50	10	0.134	0.070
			15	0.264	0.051
			20	0.265	0.034
			30	0.187	0.085
2	40	150	10	0.492	0.755
			15	0.423	0.455
			20	0.080	0.107
			30	0.101	0.120
3	60	110	10	0.730	2.299
			15	0.271	0.530
			20	0.165	0.111
			30	0.165	0.171
4	100	50	10	0.873	0.954
			15	0.205	0.793
			20	0.644	0.588
			30	0.849	0.890
5	100	70	10	0.920	1.275
			15	0.305	1.003
			20	0.706	0.440
			30	0.846	0.978
6	100	150	10	0.265	1.234
			15	0.302	1.174
			20	0.215	0.182
			30	0.893	0.945

Table 4
GRMS of the stabilizer-free BHA under various drilling parameters.

Number	Rotational speed, rpm	WOB, kN	GRMS, g
1	40	50	0.490
2	40	150	0.884
3	60	110	2.650
4	100	50	0.961
5	100	70	3.890
6	100	150	0.271

collisions involving under-gauge stabilizers become the primary excitation source for vibrations. This implies that the vibration suppression effects related to stabilizer positioning and the advantages of under-gauge stabilizers become pronounced only when drilling parameters induce severe lateral vibrations. However, controlling such intense vibrations is more practical than suppressing minor vibrations. Additionally, given the irregular curvature of wellbore trajectories, full-gauge stabilizers pose a greater risk of sticking during tripping operations. Therefore, incorporating under-gauge stabilizers into the BHA can be considered an effective optimization strategy for safe and efficient drilling in ultra-deep wells.

In addition to optimizing the stabilizer placement and sizing parameters, two other effective methods for lateral vibration suppression include the following: 1) A dual-stabilizer pendulum BHA is used. 2) Implementing the light WOB and low rotational speed drilling technique (i.e., drilling with reduced WOB and rotational speed). On the basis of the dominant factor analysis conducted in this study, both methods can further mitigate downhole vibration issues in ultra-deep wells. However, field experience indicates that the dual-stabilizer approach may increase the risk of tripping obstruction, whereas the light WOB technique inevitably sacrifices ROP, making it a relatively conservative technical choice.

4. Conclusions and future work

This study established a dynamic model for the lateral vibrations of ultra-deep well drill strings based on Cosserat geometrically exact beam theory, systematically revealed the vibration mechanisms under several dominant controlling factors, and proposed innovative vibration control strategies. The main conclusions, limitations, and outlooks are as follows:

Drill string vibration patterns are jointly influenced by rotational speed and WOB. High rotational speed conditions are more likely to induce backward whirling, whereas the effect of WOB is constrained by the critical buckling load. When the WOB remains below this threshold, increasing either rotational speed or WOB promotes backward whirling, accompanied by sharply increased vibration acceleration and bending stress. When the WOB exceeds the critical buckling load, the BHA transitions into a dynamic modal competition between buckling and whirling, leading to significantly reduced vibration intensity and bending stress. This finding provides a theoretical explanation for existing engineering practices and enables parameter optimization through mechanistic understanding. Critical buckling loads can be estimated using analytical formulas or commercial software manuals to avoid hazardous WOB ranges. Furthermore, adjusting WOB and rotational speed to achieve this low-risk modal competition maintains drilling efficiency while reducing failure probability.

The effectiveness of vibration mitigation initially increases and then decreases as stabilizers are moved upward along the drill string, while variations in outer diameter notably alter the vibration transmission patterns. Full-gauge stabilizers primarily exhibit forward whirling, demonstrating high sensitivity to the installation position. When driven by adjacent drill strings into backward whirling, severe wellbore damage may occur. In contrast, under-gauge stabilizers are more effective at suppressing severe lateral vibrations, show reduced sensitivity to installation positioning, and enhance drill string safety by promoting stress dispersion. The underlying mechanism involves irregular motion generating low-frequency transverse wave disturbances that effectively disrupt vibration patterns in the adjacent drill strings. These findings support the synergistic optimization of BHA design and drilling parameters. Under the model constraints, the optimal configuration for 0.241 m wellbores is identified as 0.231 m stabilizers placed 15–20 m behind the bit, with a low rotational speed (40–60 rpm) and a high WOB (120–150 kN).

Under actual drilling conditions, factors such as bit-rock interaction, local dogleg severity, the use of downhole motors,

and fluid-structure coupling can also influence vibrations. As this study primarily focuses on non-bit-excited lateral vibrations, these factors were not fully accounted for in the current model. Future work will expand on this foundation by incorporating a broader range of vibrational excitations and damping mechanisms. The objective is to develop a more comprehensive theoretical framework, with particular emphasis on the vibrational coupling effects arising from bit-rock interaction. Furthermore, existing theoretical and practical studies indicate that impact drilling serves as an effective vibration-reduction and ROP-enhancement method for deep formations. Jia et al. (2022) demonstrated that oscillatory axial-torsional composite loads can destabilize drill string-wellbore contacts, thereby suppressing backward whirling, revealing the potential of impact loads to control lateral vibrations. Consequently, establishing a comprehensive formation-bit-drill string coupled system to investigate complex downhole vibrations (beyond lateral modes) under impact loading can constitute a critical research focus for ultra-deep well drilling.

CRediT authorship contribution statement

Fan Yu: Writing – review & editing, Writing – original draft, Validation, Methodology, Conceptualization. **Yun-Hu Lu:** Validation, Methodology. **Yan Jin:** Supervision, Project administration. **Wei Li:** Validation, Data curation. **Bing-Qian Lv:** Resources, Data curation. **Hong-Jian Ni:** Resources, Investigation, Funding acquisition, Data curation. **Gen-Lu Huang:** Methodology, Formal analysis, Conceptualization.

Declaration of competing interest

The author declare that they have no known competing financial interests of personal relationships that could have appeared to influence the work reported in this paper.

Acknowledgements

This work is financially supported by the National Natural Science Foundation of China (Grant No. 52404014), Petro China Tarim Oilfield Company research project (Grant No. 671023115016), and Natural Science Foundation of Shandong (Grant No. ZR2025QC495).

Abbreviations

e_x, e_y, e_z	Base vectors of the principal-axis coordinate system
$\boldsymbol{e}_X$, $\boldsymbol{e}_Y$, $\boldsymbol{e}_Z$	Base vectors of the inertial coordinate system
q_0, q_1, q_2, q_3	Euler parameters
$\boldsymbol{F}$	Principal vector, N
$\boldsymbol{M}$	Principal moment, N·m
$\boldsymbol{v}$	Linear velocity vector, m·s^{-1}
$\boldsymbol{\Omega}$	Angular velocity vector, rad·s^{-1}
$\boldsymbol{\omega}$	Curvature-twist vector, rad·m^{-1}
$\boldsymbol{f}$	Distributed force resultant vector, N·m^{-1}
$\boldsymbol{m}$	Distributed moment resultant vector, N
F_x, F_y	shear forces, N
F_z	Axial force, N
M_x, M_y	Bending moments, N·m
M_z	Torque, N·m
v_x, v_y, v_z	Projections of linear velocity, m·s^{-1}
Ω_x, Ω_y, Ω_z	Projections of angular velocity, rad·s^{-1}
$\dot{v}_x$, $\dot{v}_y$, $\dot{v}_z$	Projections of linear acceleration, m·s^{-2}
$\dot{\Omega}_x$, $\dot{\Omega}_y$, $\dot{\Omega}_z$	Projections of angular acceleration, rad·s^{-2}
Γ_x, Γ_y, Γ_z	Projections of Strain
ω_x, ω_y, ω_z	Projections of curvature-twist vector, rad·m^{-1}
f_x, f_y, f_z	Projections of distributed force, N·m^{-1}
m_x, m_y, m_z	Projections of distributed moment, N
$\boldsymbol{r}$	Radius vector of any cross-section centroid relative to origin, m
ρ_s	Density of drill string, kg·m^{-3}
J_x, J_y, J_z	Per-unit-length moments of inertia, kg·m
X_p, Y_p, Z_p	Coordinates of any cross-section centroid, m
E	Elastic modulus, Pa
G	Shear modulus, Pa
I_x, I_y	Inertia moments, m^4
I_z	Polar inertia moment, m^4
$C_{\dot{K},x}$, $C_{\dot{K},y}$	Material viscous damping coefficients for bending, N·s·m^2
$C_{\dot{K},z}$	Material viscous damping coefficient for torsional, N·s·m^2
$C_{\dot{\Gamma},x}$, $C_{\dot{\Gamma},y}$	Material viscous damping coefficients for shear, N·s
$C_{\dot{\Gamma},z}$	Material viscous damping coefficient for tensile, N·s
$f_{n,x}$, $f_{n,y}$, $f_{n,z}$	Projections of normal contact force, N·m^{-1}
$f_{f,x}$, $f_{f,y}$, $f_{f,z}$	Projections of frictional force, N·m^{-1}
$f_{c,x}$, $f_{c,y}$, $f_{c,z}$	Projections of rotational centrifugal force, N·m^{-1}
$f_{g,x}$, $f_{g,y}$, $f_{g,z}$	Projections of linear buoyant weight, N·m^{-1}
$m_{f,x}$, $m_{f,y}$, $m_{f,z}$	Projections of frictional torque, N
$m_{m,x}$, $m_{m,y}$, $m_{m,z}$	Projections of drilling fluid viscous damping moment, N
X_O, Y_O, Z_O	Wellhead coordinates, m
X_B, Y_B, Z_B	Bottom hole coordinates, m
X_A, Y_A, Z_A	Coordinates on the trajectory line that is nearest to any cross-section centroid, m
d_{PA}	Distance between point A and point P, m
k_p	Wellbore stiffness coefficient, N·m^{-1}
k_c	Collision damping coefficient, N·s·m^{-2}
u_x, u_y, u_z	Projections of the unit vector directed from point A to point P
r_w	Wellbore radius, m
r_o	Drill string radius, m
r_c	Clearance between drill string and wellbore, m
d_w	Wellbore diameter, m
$\boldsymbol{v}_r$	Relative velocity vector, m·s^{-1}
$v_{r,x}$, $v_{r,y}$, $v_{r,z}$	Projections of relative velocity vector, m·s^{-1}
μ_d	Coefficient of kinetic friction
$f_{s,x}$, $f_{s,y}$, $f_{s,z}$	Projections of static friction force, N·m^{-1}
e	Eccentricity of drill string, m
ρ_m	Drilling fluid density, kg·m^{-3}
S	Area of the drill string cross-section, m^2
τ_0	Drilling fluid yield point, Pa
μ_p	Drilling fluid plastic viscosity, Pa·s
γ	Shear rate, rad·s^{-1}
T_b	Bit reactive torque, N·m
W_b	Weight on bit, kN
R	Lateral deviation ratio
v_t	Revolution linear speed, m·s^{-1}
v_X, v_Y	Projections of linear velocity in the inertial coordinate system, m·s^{-1}
a_r	Lateral acceleration at centroid, m·s^{-2}
σ_b	Bending stress, MPa
$\omega_{0,x}$, ω_0	Projections of curvature-twist vector at the end P_0, rad·m^{-1}
$_{,y}$	Projections of curvature-twist vector at the end P_0, rad·m^{-1}
Ω_0	Fixed rotational speed at the end P_0, rad·s^{-1}
$\omega_{L,x}$, $\omega_{L,y}$, $\omega_{L,z}$	Projections of curvature-twist vector at the end P_L, rad·m^{-1}
$\Gamma_{L,z}$	Tensile strain at the end P_L

References

Al Dushaishi, M.F., 2015. Numerical and Field Data Analysis of Drill Stem Vibration.. Doctoral Dissertation. Missouri University of Science and Technology, Rolla.

Alamo, F.C., Weber, H.I., 2006. Dynamics of beams using a geometrically exact elastic rod approach. In: ASME 8th Biennial Conference on Engineering Systems Design and Analysis, pp. 111–120. Torino, Italy.

Antman, S.S., 1998. Physically unacceptable viscous stress. Z. Angew. Math. Phys. 49 (6), 980–988. https://doi.org/10.1007/s000330050134.

Antman, S.S., 2005. Nonlinear Problems of Elasticity. Springer, Berlin.

Armero, F., 2025. A new finite element interpolation of the Cosserat directors for nonlinear three-dimensional Kirchhoff rods. Comput. Methods Appl. Mech. Eng. 437, 117720. https://doi.org/10.1016/j.cma.2024.117720.

Bourgoyne, A.T., Millheim, K.K., Chenevert, M.E., et al., 1986. Applied Drilling Engineering. Society of Petroleum Engineers, New York.

Cammarata, A., Greco, L., Castello, D., et al., 2025. An implicit time integrator for Cosserat rods based on the spherical Bézier interpolation. Comput. Methods Appl. Mech. Eng. 445, 118195. https://doi.org/10.1016/j.cma.2025.118195.

Cayeux, E., Ambrus, A., 2023. Self-attenuation of drillstring torsional vibrations using distributed dampers. SPE J. 28 (5), 2094–2115. https://doi.org/10.2118/214675-PA.

Cebeci, M., Gücüyener, I.H., Kök, M.V., 2019. Analysis of sinusoidal buckling of drill string in vertical wells using finite element method. In: SPE Middle East Oil and Gas Show and Conference. SPE, Mahama, Bahrain.. D032S102R001.

Choe, Y.M., Kim, G.S., Kim, I.S., et al., 2023. Influence of torsional stick-slip vibration on whirl behavior in drill string system. Geoenergy Sci. Eng. 227, 211931. https://doi.org/10.1016/j.geoen.2023.211931.

Christoforou, A.P., Yigit, A.S., 2003. Fully coupled vibrations of actively controlled drillstrings. J. Sound Vib. 267 (5), 1029–1045. https://doi.org/10.1016/S0022-460X(03)00359-6.

Di, Q., Qin, K., Chen, T., et al., 2021. An innovative method for studying the dynamic failure mechanism of box connection of stabilizer in large diameter wellbore of ultra-deep wells. J. Petrol. Sci. Eng. 205, 108822. https://doi.org/10.1016/j.petrol.2021.108822.

Di, Q., Yang, H., Wang, W., et al., 2024a. Research advances and development trend of drill string dynamics. Petrol. Sci. Bullet. 9 (2), 224–239. https://doi.org/10.3969/j.issn.2096-1693.2024.02.017 (in Chinese).

Di, Q., You, M., Li, T., et al., 2024b. Simulation and analysis of dynamic characteristics of drilling string in extra-deep wells. Petrol. Drill. Tech. 52 (2), 108–117. https://doi.org/10.11911/syztjs.2024029 (in Chinese).

Dykstra, M.W., 1996. Nonlinear Drill String Dynamics. Doctoral Dissertation.. University of Tulsa, Tulsa.

Faghihi, M.A., Mohammadi, H., Yazdi, E.A., et al., 2024. Distributed model for the drill-string system with multiple regenerative effects in the bit-rock interaction. J. Sound Vib. 571, 118120. https://doi.org/10.1016/j.jsv.2023.118120.

Fang, H., 2016. Study on Modeling of Large Deformation Beams in Multibody System Based on Geometrically Exact Beam Theory. Master's Thesis. Dalian University of Technology, Dalian (in Chinese).

Feng, T., Vadali, M., Ma, Z., et al., 2017. A finite element method with full bit-force modeling to analyze drillstring vibration. J. Dyn. Syst. Meas. Control 139 (9), 091016. https://doi.org/10.1115/1.4036083.

Gao, D., Huang, W., 2024. Basic research progress and prospect in deep and ultra-deep direction drilling. Nat. Gas. Ind. 44 (1), 98–110. https://doi.org/10.3787/j.issn.1000-0976.2024.06.010 (in Chinese).

Goicoechea, H.E., Buezas, F.S., Rosales, M.B., 2019. A non-linear Cosserat rod model for drill-string dynamics in arbitrary borehole geometries with contact and friction. Int. J. Mech. Sci. 158, 98–110. https://doi.org/10.1016/j.ijmecsci.2019.04.023.

Goicoechea, H.E., Lima, R., Buezas, F.S., et al., 2023. Drill-string with cutting dynamics: a mathematical assessment of two models. J. Sound Vib. 544, 117364. https://doi.org/10.1016/j.jsv.2022.117364.

Goicoechea, H.E., Lima, R., Buezas, F.S., et al., 2024a. A comprehensive Cosserat rod drill-string model for arbitrary well geometry that includes the dynamics of the cutting and lateral contact. J. Sound Vib. 571, 118035. https://doi.org/10.1016/j.jsv.2023.118035.

Goicoechea, H.E., Lima, R., Sampaio, R., 2024b. How to mathematically model a drill-string: lumped or continuous models? Chaos Solitons Fractals 188, 115543. https://doi.org/10.1016/j.chaos.2024.115543.

Han, Y., Ai, Z., Kuang, Y., et al., 2019. Nonlinear dynamic modeling of drill string in horizontal well-A geometrically exact approach. J. Petrol. Sci. Eng. 172, 1133–1152. https://doi.org/10.1016/j.petrol.2018.09.022.

Heisig, G., 1993. On the Static and Dynamic Behavior of Drill Strings in Spatially Curved Boreholes. Doctoral Dissertation. Technische Universität Braunschweig, Braunschweig.

Holsaeter, A., Ambrus, A., Cayeux, E., et al., 2023. Experimental verification of vibration mitigation through a viscous damping system along the drill string. In: SPE/IADC Drilling Conference and Exhibition. https://doi.org/10.2118/212521-MS.

Huang, B., Ni, H., Jin, Y., et al., 2024. The integrated drill string dynamic model based on the lumped mass method and discrete element method. Mech. Syst. Signal Process. 221, 111723. https://doi.org/10.1016/j.ymssp.2024.111723.

Huang, B., Ni, H., Zhang, H., et al., 2025. The influencing factors and new insights of drill string whirl in vertical wells. Nonlinear Dyn. 113, 25981–26008. https://doi.org/10.1007/s11071-025-11447-y.

Huang, W., Gao, D., Liu, Y., 2016. A study of tubular string buckling in vertical wells. Int. J. Mech. Sci. 118, 231–253. https://doi.org/10.1016/j.ijmecsci.2016.09.035.

Jia, P., Zhou, B., Xue, S., et al., 2022. A dynamic method for post buckling analysis of drill string in vertical wells. J. Petrol. Sci. Eng. 214, 110334. https://doi.org/10.1016/j.petrol.2022.110334.

Kamel, J.M., Muthalif, A.G.A., Falah, A.H., 2025. A review of vertical drill-string mathematical modeling. App. Eng. Sci. 22, 100227. https://doi.org/10.1016/j.apples.2025.100227.

Kapitaniak, M., Vaziri, V., Páez Chávez, J., et al., 2017. Numerical study of forward and backward whirling of drill-string. J. Comput. Nonlinear Dynam. 12 (6), 061009. https://doi.org/10.1115/1.4037318.

Lang, H., Linn, J., 2009. Lagrangian Field Theory in Space and Time for Geometrically Exact Cosserat Rods. Kaiserslautern University, Kaiserslautern.

Lang, H., Linn, J., Arnold, M., 2011. Multi-body dynamics simulation of geometrically exact Cosserat rods. Multibody Syst. Dyn. 25 (3), 285–312. https://doi.org/10.1007/s11044-010-9223-x.

Ledgerwood, L.W., Hoffmann, O.J., Jain, J.R., et al., 2010. Downhole vibration measurement, monitoring, and modeling reveal stick/slip as a primary cause of PDC-bit damage in today. In: SPE Annual Technical Conference and Exhibition. https://doi.org/10.2118/134488-MS.

Leine, R., Van Campen, D., Keultjes, W., 2002. Stick-slip whirl interaction in drill-string dynamics. J. Vib. Acoust. 124 (2), 209–220. https://doi.org/10.1007/1-4020-3268-4_27.

Li, W., Huang, G., Yu, F., et al., 2020. Modeling and numerical study on drillstring lateral vibration for air drilling in highly-deviated wells. J. Petrol. Sci. Eng. 195, 107913. https://doi.org/10.1016/j.petrol.2020.107913.

Li, X., Gao, H., Guo, X., et al., 2024. Research progress and prospect in active and passive control of drill string vibration. Nat. Gas. Ind. 44 (6), 98–110. https://doi.org/10.3787/j.issn.1000-0976.2024.06.001 (in Chinese).

Liu, W., Ni, H., Wang, Y., et al., 2023. Dynamic modeling and load transfer prediction of drill-string axial vibration in horizontal well drilling. Tribol. Int. 177, 107986. https://doi.org/10.1016/j.triboint.2022.107986.

Liu, X., Vlajic, N., Long, X., et al., 2013. Nonlinear motions of a flexible rotor with a drill bit: stick-slip and delay effects. Nonlinear Dyn. 72 (1–2), 61–77. https://doi.org/10.1007/s11071-012-0690-x.

Liu, Y., 2006. Nonlinear Mechanics of Thin Elastic Rod – Theoretical Basic of Mechanical Model of DNA. Tsinghua University Press, Beijing (in Chinese).

Lubinski, A., 1950. Astudy of the buckling of rotary drilling strings. Drill. Prod. Prac. 178.

Moraes, L.P.P.D., Savi, M.A., 2019. Drill-string vibration analysis considering an axial-torsional-lateral nonsmooth model. J. Sound Vib. 438, 220–237. https://doi.org/10.1016/j.jsv.2018.08.054.

Ni, H., Huang, B., Jin, Y., et al., 2025. Investigation of the relationship between drillstring whirl state and rate of penetration in vertical wells: influencing mechanisms and insights. SPE J. 30 (5), 2435–2451. https://doi.org/10.2118/225455-PA.

Nüsse, P.M., Ambrus, A., Aamo, O.M., 2024. Decentralized active control of distributed damping subs for stick-slip reduction in drilling. SPE J. 30 (5), 2336–2352. https://doi.org/10.2118/217676-PA.

Nüsse, P.M., Ambrus, A., Aarsnes, U.J.F., et al., 2023. Evaluation of distributed damping subs with active control for stick–slip reduction in drilling. Geoenergy Sci. Eng. 231, 212255. https://doi.org/10.1016/j.geoen.2023.212255.

Richard, T., Germay, C., Detournay, E., 2007. A simplified model to explore the root cause of stick–slip vibrations in drilling systems with drag bits. J. Sound Vib. 305 (3), 432–456. https://doi.org/10.1016/j.jsv.2007.04.015.

Shabana, A.A., Bauchau, O.A., Hulbert, G.M., 2007. Integration of large deformation finite element and multibody system algorithms. J. Comput. Nonlinear Dynam. 2, 351–359.

Simo, J.C., Tarnow, N., Doblaré, M., 1995. Non-linear dynamics of three-dimensional rods: exact energy and momentum conserving algorithms. Int. J. Numer. Methods Eng. 38 (9), 1431–1473. https://doi.org/10.1002/nme.1620380903.

Simo, J.C., Vu-Quoc, L., 1988. On the dynamics in space of rods undergoing large motions — a geometrically exact approach. Comput. Methods Appl. Mech. Eng. 66 (2), 125–161. https://doi.org/10.1016/0045-7825(88)90073-4.

Stroud, D.R.H., Lines, L.A., Minett-Smith, D.J., 2011. Analytical and experimental backward whirl simulations for Rotary Steerable bottom hole assemblies. In: SPE/IADC Drilling Conference and Exhibition. https://doi.org/10.2118/140011-MS.

Tucker, R.W., Wang, C., 2003. Torsional vibration control and Cosserat dynamics of a drill-rig assembly. Meccanica 38 (1), 145–161. https://doi.org/10.1023/A:1022035821763.

Wang, C., Ming, C., Zhang, H., et al., 2024a. Analysis of secondary makeup characteristics of drill collar joint and prediction of downhole equivalent impact torque of Well SDTK1. Petrol. Explor. Dev. 51 (3), 608–615. https://doi.org/10.11698/PED.20240057 (in Chinese).

Wang, H., Guan, Z., Shi, Y., et al., 2018. Modeling and analyzing the motion state of bottom hole assembly in highly deviated wells. J. Petrol. Sci. Eng. 170, 763–771. https://doi.org/10.1016/j.petrol.2018.07.005.

Wang, X.Y., Wang, X., Lu, J., et al., 2024b. Automated classification of drill string vibrations using machine learning algorithms. Geoenergy Sci. Eng. 239, 212995. https://doi.org/10.1016/j.geoen.2024.212995.

Wilson, J.K., 2017. Nonlinear Drill String Modeling with Applications to Induced Vibrations in Unconventional Horizontal Wells. Doctoral Dissertation. Texas A&M University, College Station.

Wu, T., Hong, J., Liu, Z., 2013. Advances of geometrically exact 3D beam theory. China Sciencepaper 8 (11), 1126–1130. https://doi.org/10.3969/j.issn.2095-2783.2013.11.012 (in Chinese).

Xiang, C., Fang, P., Li, H., et al., 2023. Nonlinear dynamics of a drillstring system with PDC bit in curved wells based on the finite element method. Geoenergy Sci. Eng. 230, 212240. https://doi.org/10.1016/j.geoen.2023.212240.

Xie, D., Huang, Z., Ma, Y., et al., 2020. Nonlinear dynamics of lump mass model of drill-string in horizontal well. Int. J. Mech. Sci. 174, 105450. https://doi.org/10.1016/j.ijmecsci.2020.105450.

Yang, Y., Luo, L., Jasiak, M., et al., 2025. Cosserat rod-based modeling and stochastic analysis for distributed fiber optics shape-sensing. Mech. Syst. Signal Process. 241, 113457. https://doi.org/10.1016/j.ymssp.2025.113457.

Yi, M., Zhao, J., Fang, H., et al., 2024. Technology breakthrough and field application of domestically produced automatic vertical drilling system. Drill. Prod. Technol. 47 (2), 159–168. https://doi.org/10.3969/J.ISSN.1006-768X.2024.02.18 (in Chinese).

Yu, F., Huang, G., Li, W., et al., 2023. Modeling lateral vibration of bottom hole assembly using Cosserat theory and laboratory experiment verification. Geoenergy Sci. Eng. 222, 211359. https://doi.org/10.1016/j.geoen.2022.211359.

Zhang, H., Di, Q., Li, N., et al., 2020. Measurement and simulation of nonlinear drillstring stick-slip and whirling vibrations. Int. J. Non Lin. Mech. 125, 103528. https://doi.org/10.1016/j.ijnonlinmec.2020.103528.

Zhang, H., Tian, K., Detournay, E., 2024a. A high-fidelity model for nonlinear self-excited oscillations in rotary drilling systems. J. Sound Vib. 573, 118193. https://doi.org/10.1016/j.jsv.2023.118193.

Zhang, Y., Ashok, P., Aguirre, J., et al., 2024b. Fast and efficient mitigation of coupled axial torsional drillstring vibrations through state-feedback linear-quadratic-integral (LQI) control. SPE J. 29 (12), 6725–6742. https://doi.org/10.2118/223618-PA.

Zhang, Y., Ashok, P., Chen, D., et al., 2023a. A control-oriented lumped parameter drillstring dynamic model for real-time vibration mitigation and drilling optimization. In: SPE/IADC Drilling Conference and Exhibition. https://doi.org/10.2118/212453-MS.

Zhang, Y., Ashok, P., Chen, D., et al., 2024c. Coupled drillstring dynamics modeling using 3D field-consistent corotational beam elements. Geoenergy Sci. Eng. 233, 212424. https://doi.org/10.1016/j.geoen.2023.212424.

Zhang, Y., Zhang, H., Chen, D., et al., 2023b. Comprehensive review of high frequency torsional oscillations (HFTOs) while drilling. J. Petrol. Sci. Eng. 220, 111161. https://doi.org/10.1016/j.petrol.2022.111161.

Zhu, X., Li, K., Li, W., et al., 2024. Drill string mechanical behaviors of large-size borehole in the upper section of a 10000 m deep well. Nat. Gas. Ind. 44 (1), 49–57. https://doi.org/10.3787/j.issn.1000-0976.2024.01.005 (in Chinese).